Planetary Nebulae in the UWISH2 survey

T.M. Gledhill[1⋆], D. Froebrich[2], J. Campbell-White[2], A.M. Jones[1]

[1] *Centre for Astrophysics Research, University of Hertfordshire, College Lane, Hatfield AL10 9AB, UK*
[2] *Centre for Astrophysics & Planetary Science, The University of Kent, Canterbury, Kent CT2 7NH, UK*

13 June 2018

ABSTRACT

Near-infrared imaging in the $1-0\,\mathrm{S}(1)$ emission line of molecular hydrogen is able to detect planetary nebulae (PNe) that are hidden from optical emission line surveys. We present images of 307 objects from the UWISH2 survey of the northern Galactic Plane, and with the aid of mid-infrared colour diagnostics draw up a list of 291 PN candidates. The majority, 183, are new detections and 85 per cent of these are not present in H α surveys of the region. We find that more than half (54 per cent) of objects have a bipolar morphology and that some objects previously considered as elliptical or point-source in H α imaging, appear bipolar in UWISH2 images. By considering a small subset of objects for which physical radii are available from the H α surface brightness-radius relation, we find evidence that the H_2 surface brightness remains roughly constant over a factor 20 range of radii from 0.03 to 0.6 pc, encompassing most of the visible lifetime of a PN. This leads to the H α surface brightness becoming comparable to that of H_2 at large radius (> 0.5 pc). By combining the number of UWISH2 PNe without H α detection with an estimate of the PN detection efficiency in H_2 emission, we estimate that PN numbers from H α surveys may underestimate the true PN number by a factor between 1.5 and 2.5 within the UWISH2 survey area.

Key words: stars: evolution – infrared: stars – planetary nebulae: general – ISM: individual: Galactic Plane

1 INTRODUCTION

There are currently around 3 500 Galactic objects which are considered to be true, likely, or possible planetary nebulae (PNe) and these are now listed in the recently-developed HASH (Hong Kong/AAO/Strasbourg/H α) database (Parker, Bojičić & Frew 2016). The majority have been discovered at optical wavelengths by their H α emission and particularly from wide-field H α surveys of the Galactic plane, such as the SuperCOSMOS H α Survey (SHS)(Parker et al. 2005; Frew et al. 2014), the INT Photometric H α Survey (IPHAS) (Drew et al. 2005; Barentsen et al. 2014) and ongoing surveys such as the VST Photometric H α Survey (VPHAS+) (Drew et al. 2014). Searches for PNe within the SHS survey have resulted in the Macquarie/AAO/Strasbourg/H α (MASH) catalogue (Parker et al. 2006; Miszalski et al. 2008). The first release of the IPHAS PN catalogue is described by Sabin et al. (2014). However, we also know that some PNe will remain invisible to these optical surveys, due to obscuration by dust, especially in the Galactic Plane (GP). In order to extend the catalogued PN population to include these optically-obscured targets, detection at longer wavelengths, particularly the near- and mid-infrared (e.g. Cohen et al. 2011; Parker et al. 2012) will be required.

PNe and pre-PNe (objects in the preceding post-AGB evolutionary stage prior to ionization of the nebula) can be strong emitters of H_2 emission lines, particularly the $1-0\,\mathrm{S}(1)$ line at $\lambda = 2.122\,\mu$m in the near-infrared. After detection of H_2 emission in NGC 7027 (Treffers et al. 1976) a number of early surveys reported H_2 emission in known PNe (Beckwith, Persson, Gatley 1978; Storey 1984). Zuckerman & Gatley (1988) established that H_2 emission is more likely to be detected in PNe that are morphologically classified as bipolar, that these objects tend to lie at lower Galactic latitude, and by implication may derive from more massive progenitors. A more extensive imaging survey of ~ 100 PNe by Kastner et al. (1996) detected $1-0\,\mathrm{S}(1)$ emission in ~ 40 per cent of their targets. They confirmed the conclusions of Zuckerman & Gatley (1988), showing that 2/3 of bipolars in

⋆ E-mail: t.gledhill@herts.ac.uk

Downloaded from https://academic.oup.com/mnras/advance-article-abstract/doi/10.1093/mnras/sty1580/5037956
by University of Kent user
on 18 June 2018

their sample were detected in H_2 emission, compared with a detection rate of less than 1 in 5 for non-bipolars. In a sample of 15 bipolar PNe, Guerrero et al. (2000) find that objects with resolved equatorial ring structures (R-BPNe) tend to be brighter in H_2 emission, and have larger $1-0\,S(1)/Br\,\gamma$ flux ratios, than those with pinched waists and unresolved cores (W-BPNe). These results are supported by more recent work (Marquez-Lugo et al. 2015; Ramos-Larios et al. 2017).

The above-mentioned H_2 detections result from observation of previously known PNe, identified in optical surveys. The UKIRT Wide-Field Imaging Survey for H_2 (UWISH2) is an unbiased near-infrared imaging survey of the northern GP, conducted using the WFCAM wide-field camera on the UK Infrared Telescope (UKIRT). UWISH2 therefore presents the opportunity to search for new PNe candidates, identified using their near-infrared H_2 emission. The survey was completed in 2013 and covers a contiguous area of the GP from $l = 357\,^\circ$ through the Galactic Centre to $l = 65\,^\circ$, with latitudes generally within $b = \pm 1.5\,^\circ$. Additional smaller fields include the star-forming regions in Cygnus and Auriga, giving a total survey area of $\approx 287\,\mathrm{deg}^2$. A narrowband filter is used, centred on the $v = 1-0\,S(1)$ ro-vibrational line of H_2 ($\lambda = 2.122\,\mu m$, $\delta\lambda = 0.012\,\mu m$). The pixel size is 0.2 arcsec (with micro-stepping) with an exposure time of 720 s per pixel. The median seeing over the whole survey is 0.8 arcsec. The survey parameters are fully described in Froebrich et al. (2011) and Froebrich et al. (2015), hereafter F15.

The resulting catalogue of extended emission includes more than 33 000 individual features, and is described in F15. Many of these features are identified with star-forming activity, such as jets and outflows (700 individual groups of features), or appear to be associated with HII regions or known supernova remnants. F15 also identified a total of 284 groups of features that are either associated with known PNe or which are PN candidates, and these are the subject of this paper. More than half of these objects are previously unrecorded and not visible on SHS or IPHAS images, revealing a potential population of optically-obscured PN and pre-PN candidates.

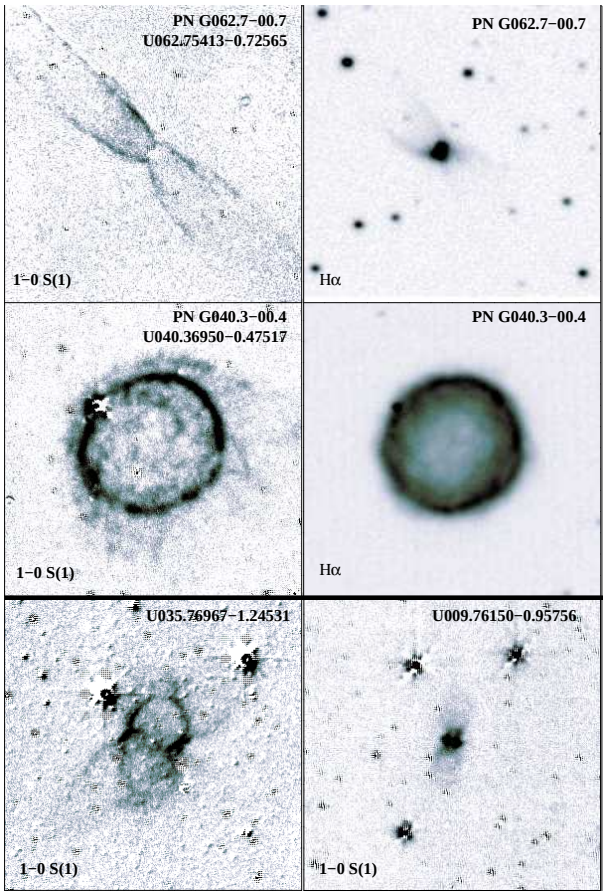

Figure 1. Example UWISH2 images. The top and middle rows show two objects which are known to be PNe with $H_2 - K$ difference images on the left and H α images, from the IPHAS survey, on the right. The bottom row shows two new PN candidates which are not detected in H α emission. The field of view in each case is 1 arcmin with North up and East left.

2 PN CANDIDATES

2.1 Candidate identification and imaging

The method for identifying H_2 emission features in the survey along with completeness estimation and rejection of contaminants is described by F15 but briefly, the following steps were followed: (i) the narrow-band images were continuum corrected by subtracting a scaled K-band image taken from the UKIDSS GPS survey (Lucas et al. 2008) to form a $H_2 - K$ difference image; (ii) the difference images were filtered to remove point sources, such as bright stars, along with large-scale variations in the background; (iii) an automated source detection algorithm was run to identify extended H_2 features with a surface brightness greater than the $5\,\sigma$ one-pixel noise and an area greater than 4 arcsec^2. The $5\,\sigma$ contour was used to define the outer bound of the emission region and the number of pixels and flux within the contour summed to give the total area on the sky and total flux of the feature. Additionally, features lying close to bright stars, within diffraction rings or within 10 arcsec of an image edge, were rejected; (iv) features separated by less than 3 arcmin were aggregated into a 'group' which is considered to be a single object. These groups were inspected to make sure that outliers around extended objects were incorporated into that group and, conversely, that nearby but obviously separate compact objects, were recorded as independent groups.

The resultant H_2 groups were examined by eye to assess whether or not they may be PNe, based on morphology, proximity to star-forming regions, association with known objects and near-infrared colour. These steps resulted in a catalogue of 284 groups (F15) that are either identified with known PNe or are considered to be PN candidates; 261 objects are located in the main survey area, 16 in Cygnus and 7 in Auriga. Fig. 1 shows example $H_2 - K$ difference images for four objects; two are known PNe and two are new PN candidates. The ability of the $H_2 - K$ images to detect faint extended H_2 emission at high spatial resolution, while simultaneously suppressing the many stellar point sources in the field, is apparent. Similar images for all our UWISH2

Downloaded from https://academic.oup.com/mnras/advance-article-abstract/doi/10.1093/mnras/sty1580/5037956
by University of Kent user
on 18 June 2018

Table 1. Summary table giving numbers of PN candidates in each morphological class.

	H α detected			H α not detected			
	Known	New	N	Known	New	N	Total
Bipolar	62	16	78	9	69	78	156
Elliptical	17	8	25	1	50	51	76
Round	6	2	8		20	20	28
Asymmetric	5	2	7	2	7	9	16
Irregular	5		5	1	8	9	14
Stellar					1	1	1
			123			168	291

PN candidates can be found in Appendix B and C (available online).

In addition to the 284 objects mentioned above, we have searched for nebulosity that may be associated with PNe amongst the H_2 groupings originally classified as 'u' by F15, and thought to consist mostly of HII regions. Of 1316 such groupings we identify a further 22 objects as possible PN candidates, mainly on the basis of their morphology, including one known PN, PN G030.2+01.5. In addition we have reclassified 081.12354+1.23547 (MHO0362) from Young Stellar Object (YSO) to possible PN. We list these extra PN candidates in Table A2 in the Appendix. This gives a total of 307 extended H_2 objects.

2.2 Identification of non-PNe

Cross-checking with the SIMBAD and HASH databases shows that 2 objects are likely to be symbiotic systems and 3 are associated with HII regions. In addition, as described in Sec. 5, we have used mid-infrared colours from *Spitzer* IRAC photometry to try to identify non-PNe, with the result that a further 5 objects are classified as likely YSOs, 4 as HII regions, 1 as a symbiotic system and 1 as a likely pre-PN. A total of 16 objects are then eliminated from the PN candidate list, leaving a total of 291.

3 PN CHARACTERISTICS

All objects are listed in Table A1 with their UWISH2 identifier in the form of the Galactic coordinates of the H_2 emission centre and their status as PN or other object. We also assign a catalogue number from 1 to 307 which is used to refer to objects more concisely within this paper (e.g #156).

3.1 Morphology

Objects have been classified morphologically according to their appearance in the $H_2 - K$ images. We use the 'ERBIAS' scheme (Parker et al. 2006) which splits objects into Elliptical, Round (aspect ratio less than 5 per cent), Bipolar, Irregular, Asymmetric and Stellar (point source) groupings. A system of sub-classifiers, 'amprs' can be used to flag asymmetric, multiple, point-symmetric, ring-like and resolved (internal) structures.

A summary of the classification into basic morphological types is given in Table 1. We note those objects that have been flagged as PNe or possible PNe in the literature (Known), and those which are unrecorded prior to UWISH2 (New). The majority of objects are bipolar 156 or 54 per cent) with 85 of these being new detections. The remaining objects are mostly in the elliptical or round category (104 or 36 per cent in total) and of these 77 per cent are new detections. There are relatively few objects in the remaining asymmetric, irregular or stellar categories (31 or 11 per cent in total).

3.2 Hα emission

The UWISH2 area overlaps with the SHS (Parker et al. 2005) in the Galactic Centre and inner GP regions out to $l \approx 35\,^\circ$, and with the IPHAS (Drew et al. 2005) for $l > 29\,^\circ$, so that any point in UWISH2 is contained within one or both of these H α surveys. We have searched for H α emission for each of our H_2 PN candidates and, if found, extracted the image to compare emission extent and morphologies. In a few cases (e.g. for fields which overlap with SHS) better quality H α images were available from other surveys such as the "IAC Morphological Catalog of Northern Galactic Planetary Nebulae" (Manchado et al. 1996) or from *HST* imaging. H α images are shown alongside H_2 images for individual objects in Appendix B.

Objects are divided into two main groups: those that are detected in H α surveys and those that are not detected in these surveys, as shown in Table 1. Of the 291 H_2 emission-line objects identified as PNe candidates in the UWISH2 survey, the majority (183) are not previously recorded and more than 85 per cent of these (155) are not detected in H α. This is perhaps not surprising, given that the principal discovery technique for PNe has been identification in H α surveys. However, we also find 28 objects for which H α emission is detected, but which have not been noted previously in the literature.

In Fig. 2 we show graphically the number of H_2-detected PN candidates, in each morphological category and whether they are visible in IPHAS and/or SHS H α surveys. Half of the objects in the bipolar category with H_2 emission also have a H α detection, whereas in the elliptical, round and other categories the majority of our H_2-detected PNe candidates are not detected in the H α surveys.

Morphological classification is clearly subjective to some degree, but where objects are detected in both UWISH2 and H α surveys, we can compare their morphological classification in the two emission lines. This is summarised in Table 2. We see that of the 50 objects classed as bipolar (B) according to their H α emission, 44 (or 88 per cent) also appear bipolar in their H_2 emission, confirming that H_2 imaging provides a comparable diagnostic of PN structure in these cases. Conversely, of the 77 objects classed as bipolar in H_2, 44 (57 per cent) are bipolar in H α, with

Downloaded from https://academic.oup.com/mnras/advance-article-abstract/doi/10.1093/mnras/sty1580/5037956
by University of Kent user
on 18 June 2018

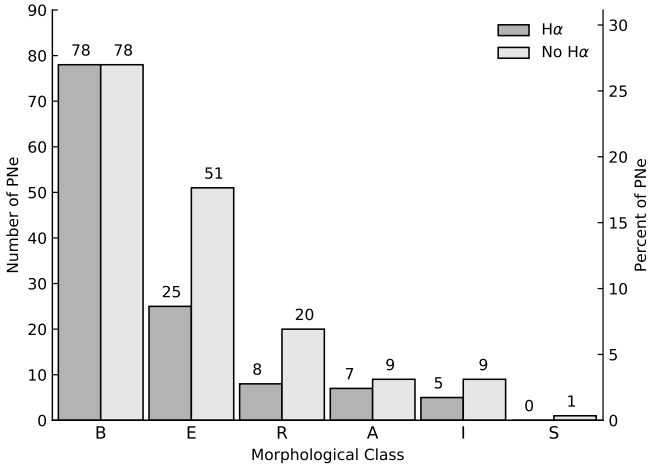

Figure 2. Graphical representation of the number of H_2-detected PN candidates in each morphological class, divided between those appearing in (darker bars) Hα surveys, with the number in each group at the top of the bar.

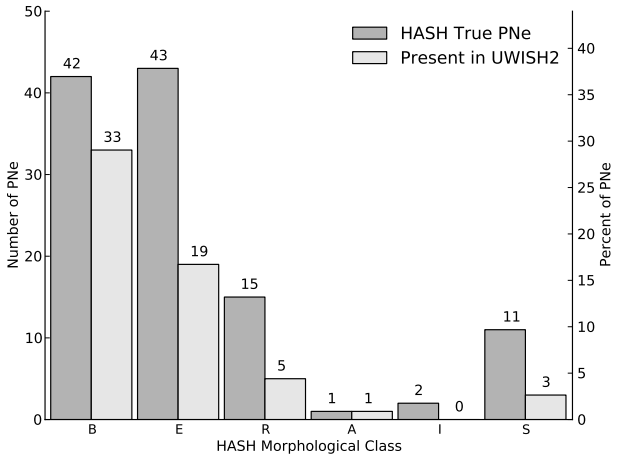

Figure 3. The sample of 'True' PNe from the HASH database in the region $66^\circ > l > 10^\circ$ and $|b| < 1.5^\circ$, grouped according to their morphological class as given in HASH (dark grey). The number of PNe in each class with a positive detection in UWISH2 is shown in light grey.

20 (26 per cent) and 8 (10 per cent) classed as elliptical and stellar, respectively. There are two likely reasons for this: (i) recombination emission often originates from the central regions of PNe, especially in young objects, so may not reflect the larger-scale structure of the PN. For example, the H α emission may highlight the central waist of a larger bipolar outflow seen in molecular emission; (ii) the spatial resolution of the UWISH2 survey (median seeing 0.8 arcsec) is greater than that of the IPHAS, and especially the SHS, so that structure seen in H_2 may remain unresolved in H α images in the case of compact objects.

3.3 Fraction of known PNe detected in UWISH2

To assess the fraction of previously recorded PNe that are detected in H_2, we select objects from the HASH PN database (Parker, Bojičić & Frew 2016) in the region $66^\circ > l > 10^\circ$ and $|b| < 1.5^\circ$, where there is a fairly uniform coverage in UWISH2. We consider only objects classed as 'True' (T), 'Likely' (L) or 'Possible' (P) PNe, discarding other non-PN classes, leaving 287 objects, of which 114 are T, 48 are L and 125 are P. The number of objects with a positive H_2 detection is 85, with 61 (54 per cent), 15 (31 per cent) and 9 (7 per cent) for T, L and P respectively. More than half of the spectroscopically confirmed (T) PNe in this region of the GP have H_2 emission. Given the low fraction of H_2 detection (7 per cent) in the case of 'Possible' PNe, it seems likely that a large fraction of these objects are not PNe.

We group the T PNe according to their morphological class as given in the HASH database, which is mostly determined by their appearance in H α imaging. We find that 33 out of 42 bipolar PNe are found in UWISH2 (79 per cent), with a lower fraction of detections amongst E, R and S classes (Fig. 2).

Given that only 9 of the HASH bipolar 'True' PNe in the selected region are absent from UWISH2, it is worth looking at these more closely. Two objects would not have been detected; PN G032.9-01.4 lies just off a UWISH2 tile, so is not included in the survey, whereas PN G026.9-00.7 is located too close to a bright star and associated diffraction pattern. A further two objects, PN G020.9-01.1 (M1-51) and PN G029.2+00.0 appear in the UWISH2 narrow-band H_2 images, but are negative in their H_2–K difference image so have not been flagged as detections. This is most likely due to strong Br γ emission in the K-band, so that we cannot say for sure if H_2 emission is present or not. The remaining 5 objects (PN G026.0-01.1, PN G027.4-00.9, PN G042.7+00.8, PN G045.7+01.4 and PN G063.5+00.0) are not detected, so the fraction of HASH True PN with bipolar morphology detected in UWISH2 could be as high as 37/42, or 88 per cent.

Table 2. A comparison of morphological classification for objects detected in both UWISH2 and H α surveys.

		H α classification					
		B	E	R	A	I	S
H_2 classification	B	44	20	1	2	2	8
	E	2	14	8	1	0	0
	R	2	2	4	0	0	0
	A	1	2	1	2	0	1
	I	1	1	1	1	1	0
	S	0	0	0	0	0	0

There is a subtlety here though, in that the H α morphology does not map directly onto the H_2 morphology. As mentioned, a significant number of objects with E or S morphologies as determined from their H α emission, appear bipolar in H_2 emission (Table 2) when observed with higher spatial resolution. This could have the effect of increasing the number of bipolar PN that are not detected in UWISH2. It has also been noted that H_2 morphology often correlates more closely with structure seen in [O I] 630.0 nm (Beckwith et al. 1978) and [N II] 658.3 nm (Fang et al. 2018), than with H α.

Downloaded from https://academic.oup.com/mnras/advance-article-abstract/doi/10.1093/mnras/sty1580/5037956
by University of Kent user
on 18 June 2018

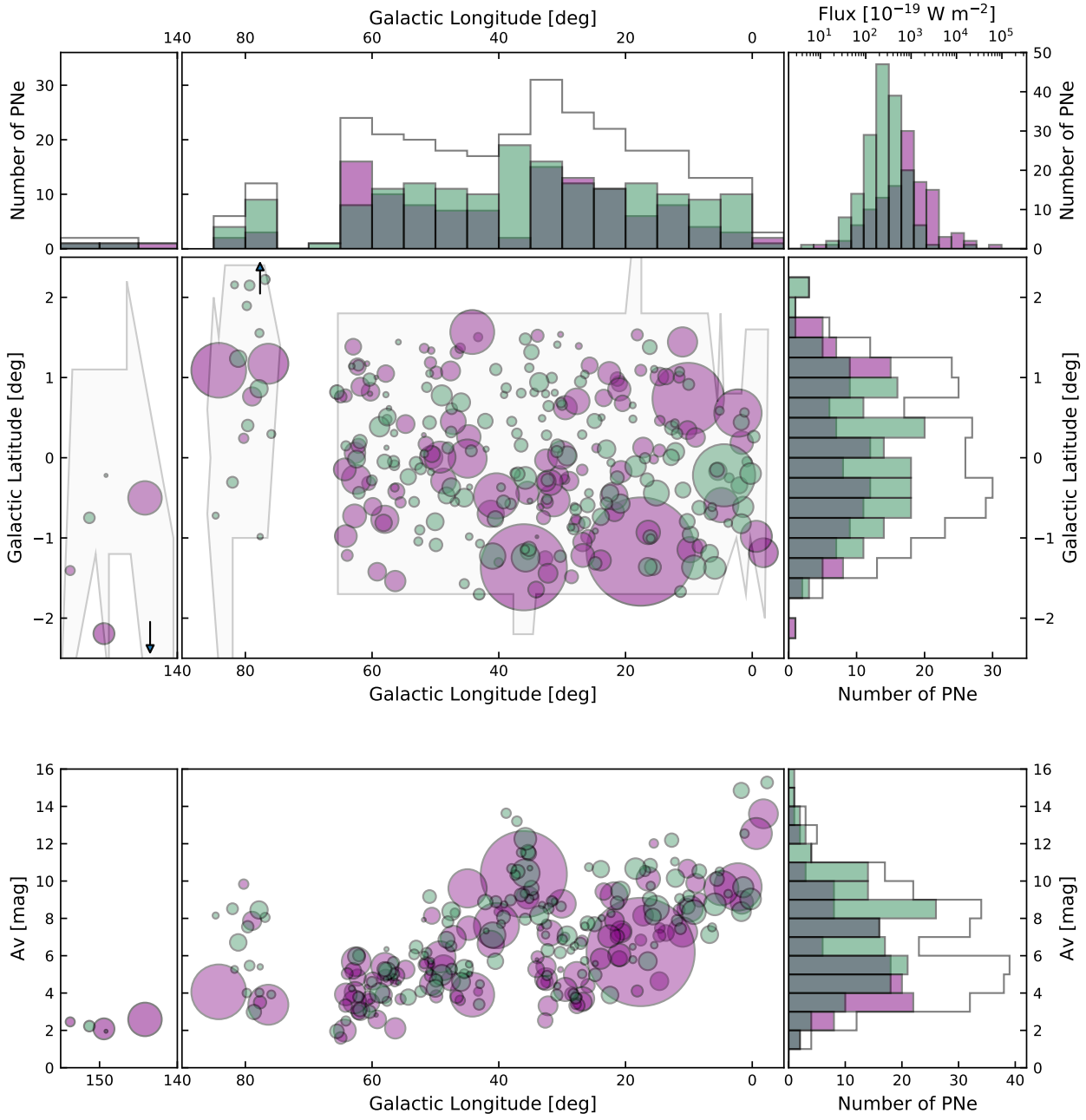

Figure 4. The top portion of the diagram shows the distribution of H_2-detected PN candidates in Galactic coordinates. Objects detected in H α emission are coloured purple and those not detected, green. The circle diameter is proportional to the area of H_2 emission on the sky (given in F15). The main survey area is shown, along with the smaller fields in Cygnus and Auriga, with grey polygonal outlines indicating the survey footprint. Arrows indicate two objects lying off the plot in latitude. Histograms of the longitude and latitude distribution also show the total PN numbers as a stepped black line. The flux distribution is shown in the top right. The lower diagram shows an estimate of the extinction at the sky position of each object as a function of Galactic longitude, with the distribution to the right.

Downloaded from https://academic.oup.com/mnras/advance-article-abstract/doi/10.1093/mnras/sty1580/5037956
by University of Kent user
on 18 June 2018

3.4 Spatial distribution

The spatial distribution of H_2-detected PN candidates is shown in the upper diagram of Fig. 4. The general distribution was discussed by F15 who noted that while a KS test gives a probability of 96 per cent that the distribution of PN in Galactic longitude is homogeneous, there are approximately 10 per cent fewer PN per unit area in the inner GP ($l < 30°$) than the outer GP, suggesting that this may be due to increased extinction towards these sightlines. The Galactic latitude distribution is more difficult to determine due to the limited coverage of UWISH2 in this direction but a scale height of $0\,°.92 \pm 0\,°.11$ was determined by F15, with the zero point coincident with $b = 0.0$ within uncertainties. The distribution of total PN number with l and b is shown in Fig. 4 by the black stepped lines in the longitude and latitude histogram panels. The total PNe candidate number per longitude bin increases gradually from the Galactic centre outwards, peaking at 30 objects in the range $l = 30 - 35°$, before dropping sharply to below 20 and then resuming a gradual increase.

The breakdown into objects with and without H α detection is shown by purple and green circles respectively, with the circle size indicative of the area of H_2 emission on the sky. There are 168 objects with no H α detection (green), or 58 per cent of the total, with many seen to be small (and faint) relative to objects detected in H α. The median surface area of H_2 emission is 162 and 70 arcsec^2 for objects with and without H α detection. The distribution in Galactic longitude of objects with H α detection is noticeably different to that of objects without; there are relatively fewer PN candidates with H α detection in the inner GP ($l < 20°$) and a pronounced dip in number between 35°and 40°. The distribution with latitude shows generally more objects without H α detection at low latitudes ($-1° < b < 1°$) and the reverse trend outside this region.

3.4.1 Extinction Effects

To investigate the effect of dust obscuration on the PN spatial distributions, we have used the extinction maps of Rowles & Froebrich (2009). These maps are based on the median near-infrared colour excess of the nearest 49 stars to a given sky position, calculated from 2MASS photometry. This is converted to an estimate of A_v on a grid with spatial resolution of approximately 1 arcmin in the GP. As explained by Rowles & Froebrich (2009), the use of the median colour excess (rather than the mean) helps to reduce bias in the extinction estimate due to intrinsically red young stars, or cluster stars with colours different to foreground/background stars. However, this also means that if there are few background stars along a line of sight, then the foreground stars dominate and the extinction is underestimated. This can easily happen in highly extincted regions of the GP where there are few background stars, even in the near-infrared. To mitigate against this, we have examined the extinction map to identify discontinuous regions where the extinction jumps to lower values over a resolution element and have discounted 24 objects that lie in these regions. The remaining 267 objects are plotted in the lower diagram of Fig. 4.

As expected there is a general trend of falling A_v with increasing l, from ~ 15 mag toward the Galactic Centre to ~ 2 mag in the Auriga field. There are upward spikes of extinction in the Cygnus clouds and in the region $35° < l < 40°$, corresponding to dark clouds in the Aquilla region. The latter region in particular coincides with the dip in H α-detected PN noted above, which is therefore most likely caused by increased extinction along these lines of sight. The distribution of PN number with A_v (lower, right panel in Fig. 4) shows relatively fewer PNe with H α detections in regions characterised by higher extinction ($A_v > 5$); the median extinction for regions containing PN with and without H α detection is 5.4 and 7.2 mag, respectively.

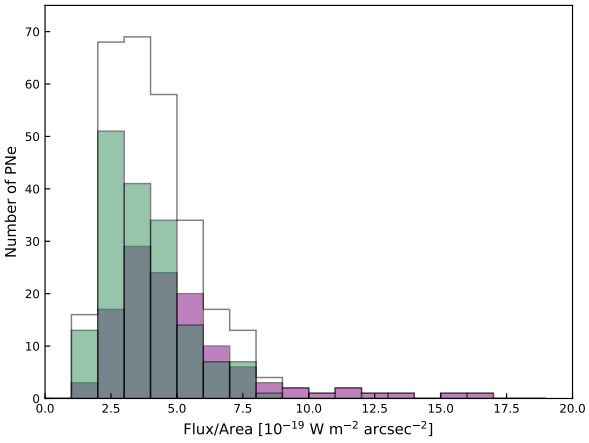

Figure 5. H_2 surface brightness distribution for objects with (purple) and without (green) H α detection. The total number is shown as a stepped black line. The $F_{\rm med}$ flux estimator is used to reduce the sparse tail of objects at high flux due to residual star subtractions (see text).

3.5 Flux and Surface Brightness Distribution

The background-corrected H_2 emission in each object can be summed over all regions lying above the 5σ pixel noise contour in the $H_2 - K$ difference image, to give a total flux, $F_{\rm tot}$. However this method can lead to an over- or under-estimate in cases where the 5σ contour includes positive or negative residuals, usually due to imperfect bright star subtraction. This can be a particular problem for very extended objects. An alternative method is to sum the median flux over the object (i.e. the median flux of a region multiplied by its area) to give $F_{\rm med}$. This will be less biased by point source subtraction errors, but is likely to underestimate the flux in objects where most of the H_2 emission arises from compact regions, such as knots and rims, which are common in our targets. Hence both methods have their drawbacks (see F15 for a more detailed comparison).

The $F_{\rm tot}$ flux distributions for objects with and without detectable H α emission are shown, on a log scale, in the top right panel of Fig. 4. The two distributions are clearly different, with a pronounced peak due mostly to fainter objects not detected in H α, and with the peak of the H α-detected sample lying at higher flux. The bright tail

Downloaded from https://academic.oup.com/mnras/advance-article-abstract/doi/10.1093/mnras/sty1580/5037956
by University of Kent user
on 18 June 2018

of the flux distribution will include some objects with over-estimated flux due to stellar residuals as described above. The median values for the flux distributions with and without detected H α emission are 9.1×10^{-17} and 3.2×10^{-17} W m^{-2}, respectively, independently of whether $F_{\rm tot}$ or $F_{\rm med}$ is adopted. This strongly suggests that UWISH2 is detecting a population of new and faint objects which are not visible in H α emission and which, in combination with the larger extinction towards these objects, are likely to be optically-obscured PN candidates.

The surface brightness (i.e. H_2 flux divided by area of emission on the sky) is, however, very similar across the UWISH2 sample, regardless of H α detection, and is shown in Fig. 5. The median surface brightness is 3.9×10^{-19} W m^{-2} arcsec^{-2}, and is again independent of whether the $F_{\rm tot}$ or $F_{\rm med}$ flux estimator is adopted. The narrow distribution in surface brightness (neglecting a few bright objects detected in H α) means that fainter objects tend also to have smaller angular extent, and suggests that the difference in the median flux of the objects with and without H α detection (Fig. 4) is due to the latter being, on average, at larger distance. This is again consistent with the idea that the near-infrared UWISH2 survey is probing longer sight lines to more distant and reddened objects.

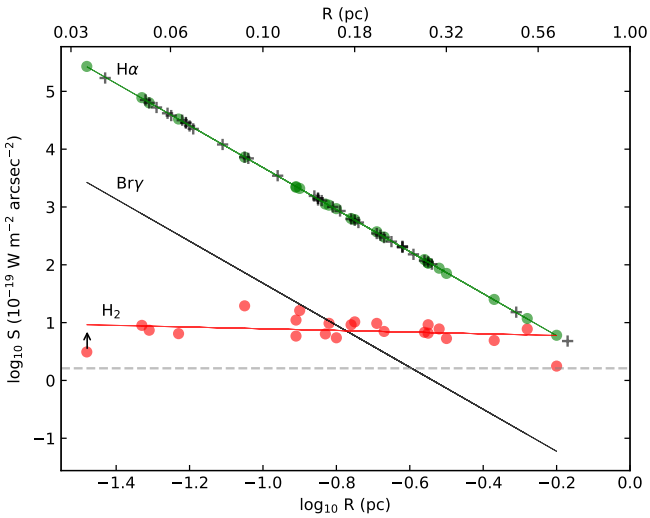

Figure 6. Surface brightness against radius for 23 PNe in common between UWISH2 and FPB16 with green circles showing H α emission and red circles $1-0$ S(1) emission. Lines of best fit are also shown. The Br γ trend is obtained by shifting the H α fit line down by 2 dex. PNe from FPB16 which are within the UWISH2 area but not detected in H_2 are shown as black 'plus' symbols. The H_2 surface brightness detection limit is shown as a dotted line (see text for details).

4 SURFACE BRIGHTNESS-RADIUS RELATIONSHIPS

The relationship between the H α surface brightness and physical radius of an ionized nebula has been used to derive distances to more than 1000 PNe (Frew, Parker & Bojičić 2016, hereafter FPB16). The relationship arises due to the H α flux scaling with the nebula volume (i.e. with the cube of the radius, r) and the emissivity, which for recombination line emission depends on the square of the electron density, $n_{\rm e}$. The surface brightness, S, is independent of distance and scales as $rn_{\rm e}^2$. Assuming a power law $n_{\rm e} \propto r^{\alpha}$ then $S \propto r^{2\alpha+1}$. FPB16 find $S_{\rm H\alpha} \propto r^{-3.6}$ for a sample of calibration PNe for which the distances (and hence radii) are independently known.

There are 23 PNe for which FPB16 derive radii and distances based on their extinction-corrected H α surface brightness, and which also appear in UWISH2 (Table 3). $S_{\rm H\alpha}$ for these objects is plotted in Fig. 6 as green circles, and by definition they lie on a straight line of slope -3.6 in a log-log plot, as their physical radii have been estimated assuming the above H α surface brightness-radius ($S_{\rm H\alpha} - r$) relationship. The 38 objects listed in FPB16 which are within the UWISH2 survey area, but not detected in H_2, are shown as black 'plus' symbols and listed at the foot of Table 3. The dotted horizontal line shows an indicative H_2 surface brightness detection limit of 1.62×10^{-19} W m^{-2} arcsec^{-2}, based on the median pixel noise for the UWISH2 survey (note that the actual pixel noise varies across the survey; see F15 and their fig. 4 for details). The red circles show the $1-0$ S(1) surface brightness (i.e. $F_{\rm med}$ divided by area of H_2 emission) for the detected objects. In order to correct the H_2 data for extinction, for comparison with the de-reddened H α data, we use the same $E(B-V)$ colour excess given by FPB16. We assume a ratio of total to selective extinction $A_{\rm V}/E(B-V) = 3.1$ and a power-law near-infrared extinction curve with index -1.95 (Wang & Jiang 2014).

The H_2 surface brightness-radius ($S_{\rm H_2} - r$) relation, unlike the H α emission, appears roughly flat over a factor of 20 in nebula radius, from 0.03 to 0.6 pc. The best-fit line shown has a gradient of -0.14. This range of radii is expected to encompass most of the visible (optical emission line) lifetime of a PN (Jacob et al. 2013), ranging from young, bright, and compact objects on the left to extended, faint and old objects to the right. Note that the radius here is that of the ionised region and the H_2 emission may extend out to larger radius in the form of a molecular envelope. The objects with smallest and largest radius, #214 and #252, have low surface brightness compared to the average trend. Object #214 has intense Br γ emission from a compact region in the centre; this leads to over-subtraction in the $H_2 - K$ difference image and a likely under-estimate of the H_2 flux, so that this point is a lower limit to the true surface brightness. In the case of #252, the H_2 emission is genuinely very faint, possibly indicating that in the most extended and presumably most evolved objects, little molecular material remains. Neglecting these two outliers, the mean H_2 surface brightness is $8.6 \pm 3.6 \times 10^{-19}$ W m^{-2} arcsec^{-2} over a factor of 10 range in PN radius, from 0.05 pc to 0.5 pc.

The similarity of H_2 surface brightness in objects covering such a large range of radii suggests that, unlike H α, the H_2 emission does not originate throughout the volume of the PN and does not scale in the same way with radius. This is consistent with many of our UWISH2 images (Appendix B and C) which show that H_2 emission often arises from thin structures at the extremities of PNe, such as cavity walls and edges in bipolar objects, and rims and shells in more elliptical objects. This has been noted in previous studies (e.g. Guerrero et al. 2000; Fang et al. 2018) and is particularly evident in #161 (PN G040.3-00.4;

Downloaded from https://academic.oup.com/mnras/advance-article-abstract/doi/10.1093/mnras/sty1580/5037956
by University of Kent user
on 18 June 2018

Table 3. 23 UWISH2 PNe with radii (in increasing order) taken from FPB16. The ratio of Br γ to H_2 surface brightness is estimated by scaling the H α surface brightness, as explained in the text. The value for #214 is an upper limit. Median H_2 flux, $F_{\rm med}$, is in units of 10^{-19} W m^{-2}. The PN G numbers of 38 objects in FPB16 which are within the UWISH2 area but not detected in H_2 are shown at the bottom of the table.

Object #	Other Name	$\log_{10} r$	$S_{Br\gamma}/S_{H_2}$	$F_{\rm med}$
214	M 1-71	-1.48	1.24e3↓	139↑
026	NGC 6537	-1.33	1.06e2	20 474
021	M 1-40	-1.31	7.17e1	552
098	M 2-45	-1.23	8.04e1	1 557
284	Hb 5	-1.05	2.73e0	8 645
087	Pe 1-14	-0.91	2.37e0	858
262	KjPn 2	-0.91	4.36e0	414
074	MaC 1-13	-0.90	1.69e0	3 279
072	M 3-28	-0.83	2.23e0	2 075
071	M 3-55	-0.82	1.31e0	1 480
280	K 3-65	-0.80	2.16e0	202
131	CBSS 3	-0.76	8.92e-1	698
161	Abell 53	-0.75	6.52e-1	9 475
128	Te 7	-0.69	5.23e-1	1 552
118	HaTr 10	-0.67	5.26e-1	3 019
044	PHR J1813-1543	-0.56	2.07e-1	882
259	Abell 69	-0.55	1.44e-1	4 463
272	K 4-55	-0.55	2.17e-1	12 704
120	WeSb 4	-0.52	1.40e-1	2 182
147	Sh 2-71	-0.50	1.45e-1	9 476
047	PHR J1818-1526	-0.37	5.97e-2	178
165	HaTr 14	-0.28	1.55e-2	2 883
252	Te 1	-0.20	3.73e-2	108
000.1-01.7, 000.2+01.7, 000.3-01.6, 000.6-01.3, 000.7-01.5, 000.8+01.3, 000.8-01.5, 000.9+01.1, 000.9-01.2, 001.0+01.3, 001.1-01.6, 001.2-01.2a, 001.3-01.2, 010.0-01.5, 011.7+00.0, 011.7-00.6, 013.3+01.1, 015.5+01.0, 017.5+01.0, 019.6+00.7, 019.9+00.9, 020.2-0.06, 020.9-01.1, 027.0+01.5, 027.5+01.0, 029.0+00.4, 036.9-01.1, 056.4-00.9, 058.9+01.3, 060.5-00.3, 065.9+00.5, 151.4+00.5, 358.9-00.7, 359.1-01.7, 359.2+01.3, 359.3-01.8, 359.5-01.2, 359.7-01.4				

Abell 53), shown in Fig. 1, where the H_2 emission arises mainly from a thin circular ring. Assuming that the object is a spherically symmetric PN, rather than a bipolar viewed exactly pole-on, then this corresponds to a thin shell at the outer boundary of the ionised region, the extent of which is indicated by the H α image. This is also consistent with, for example, the spherically-symmetric photoionization models of Aleman & Gruenwald (2011) which show that the most significant contribution to $1-0$ S(1) emission occurs in a relatively thin transition zone (TZ) outside the fully ionised region. They define the TZ to be a shell of warm, partially ionised gas, where the fraction of ionized hydrogen drops below 0.95 and find that the $1-0$ S(1) emissivity, j, rises to a maximum in this region. We note, however, that these models do not include a molecular envelope outside the ionized region, or shock excitation of the H_2 molecule, which is known to be important, especially in bipolar objects (e.g. Kastner et al. 1996; Marquez-Lugo et al. 2015). In fact, there is mounting evidence that the relative importance of shocks and fluorescence depends on PN age, with shocks being prevalent in early and late phases of PN evolution (Davis et al. 2003; Ramos-Larios et al. 2017).

Fig. 6 shows that for PNe with large radii ($r > 0.5$ pc) the H_2 and H α surface brightnesses become comparable. If the angular extents in both lines are also similar, a reasonable assumption for evolved objects where the ionisation front will have overtaken most of the molecular envelope, then the H_2 and H α fluxes should also be similar. In these cases, detection of extended PNe using their H_2 emission may be easier, especially considering a factor of ~ 10 in differential extinction between the two lines.

We also plot the approximate Br γ surface brightness-radius relation in Fig. 5, by shifting the H α surface brightness from FPB16 (already dereddened) down by 2 dex to account for the intrinsic Br γ/ H α line ratio[1]. Due to the flat trend in H_2 surface brightness, the ratio of Br γ to H_2 surface brightness also varies with nebula radius, with the two being comparable for a radius of approximately 0.17 pc, as shown by the intersection of the two best-fit lines (Fig. 6). Smaller PNe have $S_{Br\gamma} > S_{H_2}$ and larger PNe have $S_{Br\gamma} < S_{H_2}$, for the range of radii shown. The ratios computed from our UWISH2 $1-0$ S(1) surface brightness and the estimated Br γ surface brightness are given in Table 3.

5 MID-INFRARED COLOURS

Cohen et al. (2011) discuss the *Spitzer Space Telescope* IRAC colours of 136 optically-detected and spectroscopically-confirmed PNe from the MASH catalogue, as part of a multi-wavelength approach to the characterization of PNe. They present IRAC colour-colour planes as diagnostic tools to aid discrimination of PNe from contaminants which can appear similar at optical wavelengths, such as diffuse and compact HII regions (see also Zhang et al. 2012). This approach also offers the possibility to identify PNe on the basis of their mid-infrared emission, by comparing their IRAC colours with those of optically-confirmed PNe. For UWISH2 objects this is advantageous given that the majority of our new PN candidates are not optically visible and therefore cannot be confirmed using the usual optical diagnostic lines.

To determine the IRAC colours of our UWISH2 objects we extract cut-outs from the GLIMPSE survey[2] centred on the coordinates of each object, and with a cut-out size determined by the extent of the H_2 emission. Where emission is seen above the diffuse background level we then measure the flux using elliptical apertures to encompass all of the emission. The sky background is estimated by offsetting the aperture to a region of diffuse background. Any point sources within the apertures are subtracted from the aperture sum (unless within the object aperture and associated with the source). We have applied the extended source correction factors[3] which depend on aperture size;

[1] The value of $\log(Br\gamma/H\alpha)$ varies weakly with gas temperature and density but is -2.0 ± 0.1 for values in the range $10^3-3\times10^4$ K and 10^2-10^4 cm^{-3} respectively (Hummer & Storey 1987).
[2] `http://irsa.ipac.caltech.edu/data/SPITZER/GLIMPSE/index_cutouts.html`
[3] The procedure for IRAC extended source calibration is given by T. Jarrett at `http://www.ast.uct.ac.za/~jarrett/irac/calibration/index.html`

Downloaded from https://academic.oup.com/mnras/advance-article-abstract/doi/10.1093/mnras/sty1580/5037956
by University of Kent user
on 18 June 2018

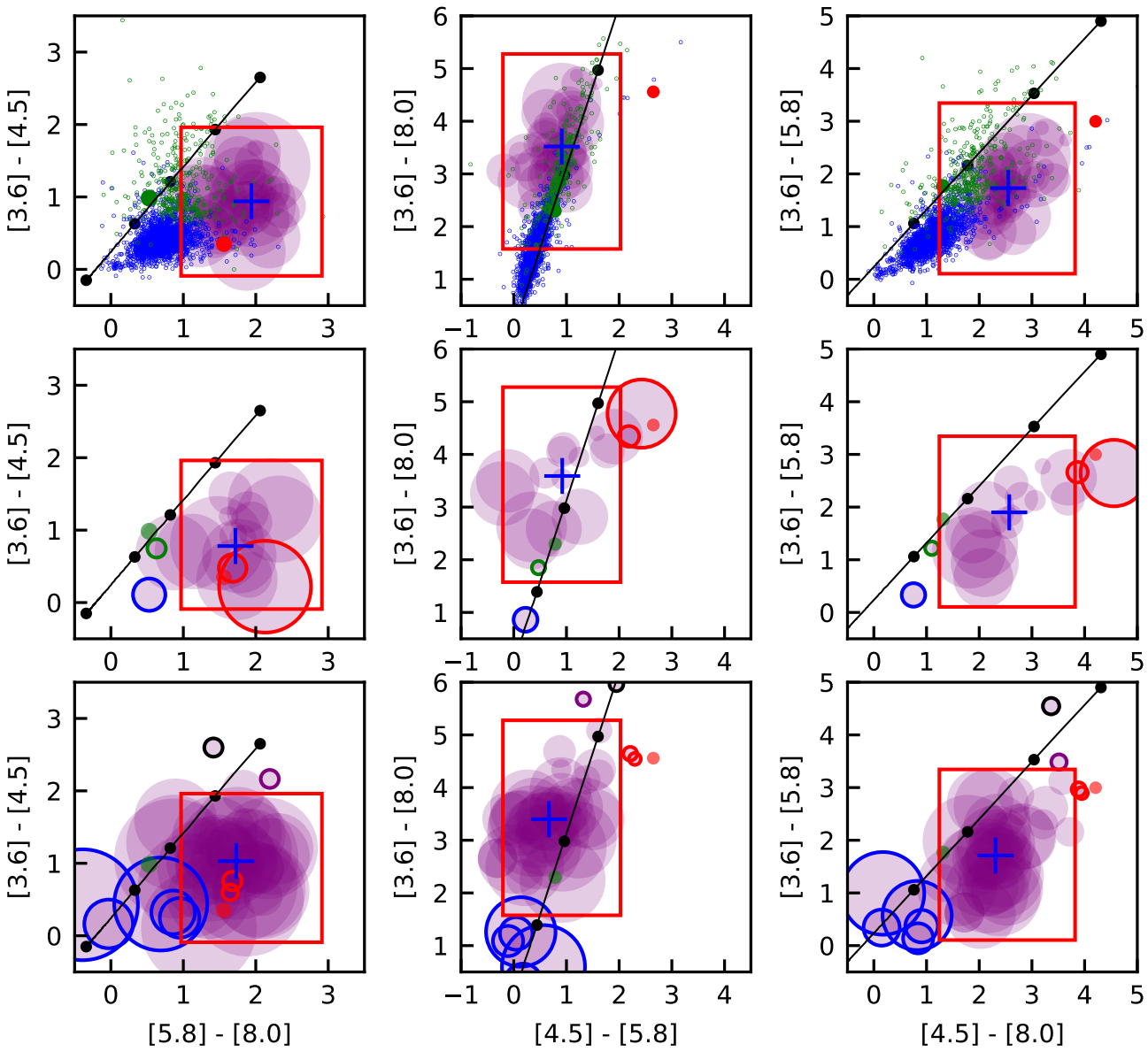

Figure 7. *IRAC* colour-colour plots for UWISH2 PN candidates shown as filled purple circles with circle diameter indicative of the photometric errors. *top row:* 33 objects flagged as "True PNe" in the HASH database; *middle row:* 18 PN candidates with H α detection; *bottom row:* 45 PN candidates not detected in H α. Black lines show blackbody colours with temperature varying from 300 K (top right) to 10 000 K (bottom left) with points marked at 300, 400, 600, 1 000 and 10 000 K. In each plot the median colour is shown as a blue cross with ± 3 standard deviations in colour shown by the red rectangles. The red and green filled circles correspond to PN G014.9+00.0 and PN G050.4+00.7, a HII region and candidate symbiotic system, respectively. Additionally in the top row we plot data from Megeath et al. (2012) showing the locations of YSOs as small blue and green circles (corresponding to disk sources and protostars respectively).

where an aperture radius less than 8 arcsec is used then no correction is applied. Errors on the photometry are estimated simply from the counts in the object and sky apertures. Where the emission is faint and/or the diffuse background is high, then the errors on the IRAC colours will be larger.

We list the IRAC photometry for each object, where available, in Table A1 and give an object "type". For known objects which already have a T, L or P (true, likely or possible PN) designation, from optical spectroscopy, then this is preserved. For H_2 PN candidates that have no previous observations then by default we list these as 'c' (candidate) unless there is evidence from the IRAC photometry of a PN nature, in which case we use lower-case t, l, p designations as follows. Where photometry is available in all four bands and the six colours are consistent with PNe (see below) then we list objects as 't'. Where only three bands are available, but the three resulting colours are consistent with PNe then we list them as 'l'. If only 2 bands are available but the resulting colour is consistent with PNe then they are labelled 'p'. Where the IRAC colours are more consistent with a YSO or HII region, then they are labelled as such.

Downloaded from https://academic.oup.com/mnras/advance-article-abstract/doi/10.1093/mnras/sty1580/5037956
by University of Kent user
on 18 June 2018

5.1 True PNe

There are 76 objects in the UWISH2 sample which are classified as 'true' PNe in the HASH database. The latitude coverage of UWISH2 (generally $|b| \leqslant 1.5^\circ$ over much of the survey, but extending to higher latitude coverage in places) is larger than that of GLIMPSE ($|b| \leqslant 1.0^\circ$) so that only some UWISH2 objects appear in GLIMPSE. Of those that do, some do not have usable images in all four IRAC bands, and in some cases there is no obvious emission above the background level that can be associated with the object (i.e. lying within the area defined by the H_2 emission). Of the 76 true PNe, 33 have usable IRAC images from which flux in all four bands, and colour, can be determined. We plot these objects as purple circles in the three colour-colour planes in Fig. 7 (top row), where the PNe are seen to occupy well-defined regions. The radii of the circles are equal to the average of the uncertainties in the two colours, calculated from the photometry. The median colours of the PNe are marked with blue crosses and are listed and compared to the values of Cohen et al. (2011) in Table 4, showing consistent locations; 17/33 of the plotted PNe are present in the MASH and hence common between the two samples, the rest are in IPHAS. The likely HII region PN G014.9+00.0 (#45) and symbiotic system PN G050.4+00.7 (#195) are also plotted (red and green filled circles respectively) and occupy regions distinct from the PNe grouping in two of the three planes. We define rectangular regions in each colour plane, shown in red, centred on the median colour and with extent ± 3 standard deviations in each colour. These regions contain all of the true PNe and are therefore the regions in which PNe are expected to lie.

In addition to diffuse HII regions, which are known to make up the majority of detections in UWISH2, the other main contaminant will be from embedded young stellar objects (YSOs). In drawing up the PN list we have eliminated objects clearly associated with jets, known YSOs, or which appear clustered; the IRAC colour planes offer an additional tool to discriminate between PNe and YSOs. We plot in Fig. 7 the locations of YSOs taken from the *Spitzer* IRAC survey of the Orion A and B molecular clouds by Megeath et al. (2012). A total of 2 598 sources are plotted, for which photometry in all 4 IRAC bands is available, comprising 2 206 sources identified as pre-main sequence stars with discs and 392 protostars. We take the locations of these objects in the IRAC colour-colour planes to be typical of the locations of dusty YSOs. The [5.8]-[8.0] vs. [3.6]-[4.5] plot in particular does a good job of separating YSOs from PNe, with few YSOs occupying the PN region. The [4.5]-[5.8] vs. [3.6]-[8.0] and [4.5]-[8.0] vs. [3.6]-[5.8] colour planes show a good separation between PNe and the likely location of diffuse HII regions (red circle), with slightly more contamination of the PN region by YSOs, especially in the former case where the track of cool blackbody colours runs through the PN region.

5.2 Other optically-visible PN candidates

The IRAC colours of 18 PN candidates with detected H α emission, but which are not spectroscopically confirmed as true PNe, are shown in the middle row of Fig. 7. These include objects with 'L' or 'P' designations as well as objects newly detected in UWISH2.

One object, #234 (PN G059.7-00.8), lies outside the PN box in all three planes to the bottom left, in the region occupied by YSOs (blue-edged circle). The object has a bipolar (Bs), spider-like morphology in H_2 (Fig. B1) with a central peak. In IPHAS H α imaging it appears as a compact bright central region with a fainter halo. It is identified spectroscopically as a likely PN by Sabin et al. (2014). We have obtained *K*-band spectroscopy with *LIRIS* on the WHT which shows H_2 line ratios characteristic of thermal excitation in the nebula and evidence for the $v = 2 - 0$ and $3 - 1$ CO bandheads in absorption at the central position (Jones et al. 2018, submitted). CO bandhead absorption is seen in many YSOs, where it can arise in the photosphere (e.g. Casali & Eiroa 1996) or in the disc, especially in FU Ori type systems (Reipurth & Aspin 1997). CO absorption is also seen in the spectra of cool evolved objects, such as pre-PNe with spectral types G and later, but tends to be absent in hotter post-AGB objects (e.g. Hrivnak, Kwok & Geballe 1994). It is possible that PN G059.7-00.8 is a YSO, but given its current PN status it seems more likely to be a PN in chance alignment with a field star.

Object #283 lies outside the PN box in two colour planes and close to the blackbody track; it also lies close to the position occupied by PN G050.4+00.7, in all three colour planes (green-edged circle), which is listed as a possible symbiotic star in the HASH database, although Sabin et al. (2014) list it as a likely PN. The object has irregular (I) morphology in H_2 with a compact central source visible in the SHS H α image (Fig. B4). Its location in Fig. 7 may, therefore, indicate a symbiotic (or possibly YSO) nature rather than a PN, however we note that it is often difficult to differentiate between the two classes (Frew & Parker 2010). A particular case is Mz 3, which has been classed as PN and symbiotic and has a mid-infrared-to-radio flux ratio characteristic of HII regions (Cohen et al. 2011).

Two objects (red-edged circles) have colours similar to those of diffuse HII regions. These are #038 and #171 which have bipolar (Bp) and round (Rs) H_2 morphologies (Figs B5 and B7 respectively). The latter object is an IRAS source - IRAS 19117+0903.

5.3 Optically invisible PN candidates

There are 45 UWISH2 PN candidates with no H α detection and for which IRAC photometry in all 4 bands is obtained. These are shown in the bottom row of Fig 7. We note that the majority of objects have IRAC colours typical of PNe and that the median colours are well-centred in the box defined by the "True" PNe, so that our initial selection procedure (based on morphology and avoidance of star-forming clouds) was mostly successful.

A group of 5 objects lies to the bottom left of the colour planes, outside the PN box and in the region occupied by YSOs. These are again shown as blue-edged circles and are #014, #111, #124, #012 and #032. Three objects (#014, #111 and #124; Fig. C4) appear asymmetric in H_2 emission whereas two (#012 and #032; Fig. C1) are possibly bipolar. *K*-band spectroscopy of #012 shows H_2 line ratios typical of thermal excitation in the nebula, with no evidence of Br γ emission (Jones et al. 2018, submitted) and so is a likely

Downloaded from https://academic.oup.com/mnras/advance-article-abstract/doi/10.1093/mnras/sty1580/5037956
by University of Kent user
on 18 June 2018

Table 4. Median IRAC colours and standard error on mean (sem) for 33 UWISH2 PNe classed as "True" PNe, and the set of "All PNe" from the MASH sample of Cohen et al. (2011).

Colour	This work			MASH Sample	
	median	std. dev.	sem	median	sem
[3.6] − [4.5]	0.94	0.34	0.06	0.81	0.08
[3.6] − [5.8]	1.73	0.54	0.10	1.73	0.10
[3.6] − [8.0]	3.43	0.62	0.11	3.70	0.11
[4.5] − [5.8]	0.91	0.37	0.07	0.86	0.10
[4.5] − [8.0]	2.53	0.43	0.07	2.56	0.11
[5.8] − [8.0]	1.94	0.32	0.06	1.86	0.07

YSO. The remaining 4 objects could also be YSOs, although the IRAC images contain point sources so it is possible that these are also PNe superimposed with field stars.

Two objects have colours similar to those of diffuse HII regions (red-edged circles). These are #029 and #048 (Figs. C2 and C1 respectively). Both are bright in the IRAC bands and we consider them as likely HII regions.

Two objects lie outside the PN box in the upper part of the colour planes. The object with the more extreme colours is #066, shown with a black-edged circle. In H_2 imaging it appears as a compact bipolar consisting of two small blobs of emission (Fig. C1) with extent 2.8 × 1.2 arcsec. *K*-band spectroscopy shows no Br γ emission (Jones et al. 2018, submitted). Given the small dimensions and lack of evidence of ionization, this is likely to be a pre-PN. Object #114 is shown with a purple-edged circle and also lies outside the PN box. This object appears as an X-shaped bipolar in H_2 imaging, with a bright central star. It is a radio and millimetre source and has been listed as a PN (Urquhart et al. 2009). In a survey of the inner GP for Wolf-Rayet stars, Kanarek et al. (2015) also class this object as a possible PN (object 1527-318B); their near-infrared spectrum shows strong emission from HeI (2.058 µm) and Br γ which can be characteristic of young PNe (e.g. Gledhill & Forde 2015). These lines are also found in massive YSO spectra and HII regions, but in the case of MYSOs the continuum rises steeply into the red (Cooper et al. 2013), whereas the continuum of #114 appears flat. The IRAC images show a compact source suggesting that the object is not a diffuse HII region either. Although #114 lies outside the PN box in our colour-colour plots, we retain it as a candidate PN.

6 PNE TOWARDS OPEN CLUSTERS

A possible, although rarely available, approach to measuring the distance to a PN, along with the age of the PN progenitor, is to identify PNe in open clusters. Several studies of this type have been made but the number of confirmed cluster members is small. A summary is given by FPB16, who use 9 PN-cluster pairings as calibrators for their $S_{H\alpha} - r$ relation, including 4 PNe in globular clusters. We have hence cross-checked our list of PN candidates to identify objects that potentially could belong to open clusters.

We utilised the Milky Way Star Cluster (MWSC) catalogue by Kharchenko et al. (2013) for this purpose. This catalogue features a list of 3006 confirmed clusters

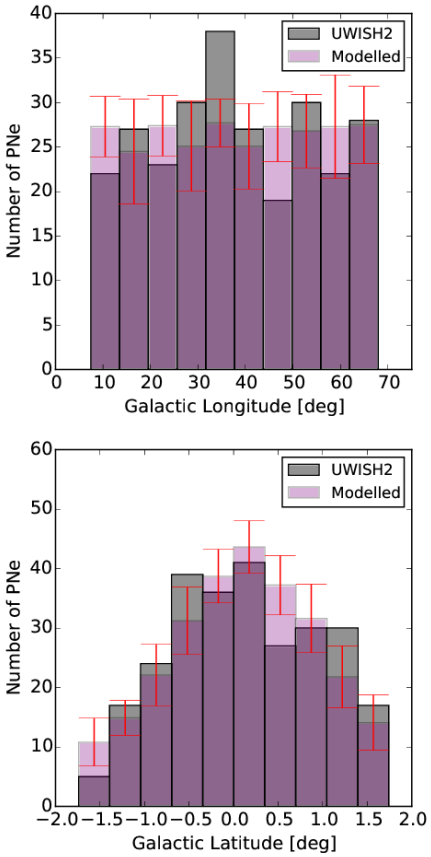

Figure 8. Observed and modelled planetary nebulae Galactic distribution histograms from UWISH2. The purple bins represent the average modelled distribution from 1000 simulations, with ±1σ error bars. The grey bins are the observed PNe from the survey ($N_{\rm PNe} = 266$).

(open, globular and associations) from a number of sources and provides a uniform and homogeneous set of cluster parameters such as positions, radii, distances and ages. We find a total of 18 PN candidates which are within the angular radius of one of the star clusters. The full list of objects and the associated clusters and their properties are shown in Table 5.

Some of these associations could be chance projections. In order to evaluate what fraction of sources could be real associations we run some basic simulations. This was only done for the core region of UWISH2, i.e. for the objects at Galactic longitudes between 0° and 65°and Galactic latitudes between ±1.7°. This region has a homogeneous coverage in UWISH2, in both coordinates. There are 15 PNe which overlap with clusters in this area. The remaining three associations of PNe and clusters occur in the additional UWISH2 fields taken in Cygnus and Auriga/Cassiopeia where no homogeneous coverage has been achieved.

In order to estimate how many associations of PNe and clusters one would expect, we randomly distribute the same number of PNe in the survey area and identify how many of them are projected onto the star clusters. We repeat this simulation 1000 times to estimate a reliable mean and uncertainty for our estimates. We also ensure that the random positions in the simulation follow the same

Downloaded from https://academic.oup.com/mnras/advance-article-abstract/doi/10.1093/mnras/sty1580/5037956
by University of Kent user
on 18 June 2018

distribution as the real PNe. In other words the Galactic longitudes are sampled from a homogeneous distribution, while the Galactic latitudes are sampled from a Gaussian distribution with a width of 0.83° and a centre position of -0.03°. In Fig. 8 we show the observed distributions in l and b, as well as the average and scatter of the simulated distributions. We do not randomise the positions of the clusters during the simulation, but keep them fixed in their real positions. The reason for this that the MWSC list has to a large extent been made by combining cluster lists from the literature. Hence, the cluster list will suffer from a non-homogeneous coverage. Thus, randomising the position may cause erroneous results.

We find that on average in our 1000 simulations there are 13.2 ± 3.6 PN projected onto one of the clusters. Hence, within the uncertainties the 15 PNe that overlap with clusters are to be expected randomly. Thus, the number of PNe that are expected to be associated with a cluster seems to be very small. We attempted to run a larger number of simulations to reduce the uncertainties, but find that the scatter is not reduced once the number of runs is above 1000. We also slightly changed the latitude distribution of the PNe in the simulation but obtain the same results for the number of associations within the error bars.

One would expect that PNe in clusters occur mostly once the age of the cluster exceeds $\sim$ 50 Myr, which corresponds approximately to the time for a 7 $M_\odot$ star to evolve to the post-AGB stage (e.g. Choi et al. 2016). Out of 15 possible associations of PNe with clusters, 5 are for clusters with ages above 100 Myr. These five (in the clusters Ruprecht 137, ASCC 94, Kharchenko 2, Kronberger 2, NGC 6649) may then be the most likely objects to be really associated with clusters.

#012: IRAC colours suggest that this object is likely to be pre-main sequence (Sec. 5.3). Distance and reddening are unknown although a median $E(B-V) = 2.6$ along this line of sight (Sec. 3.4.1) implies that it may be background to the cluster.

#290: A small (5 x 3 arcsec) bipolar, possibly associated with ASCC 94 although the cluster distance would imply an object extent of less than 0.01 pc, more typical of a pre-PN.

#071: A confirmed PN (PN G021.7-00.6; M 3-55) with $S_{H\alpha} - r$ distance of 5.86 ± 2.46 kpc and $E(B-V) = 1.61$ (FPB16) suggesting it is background to the cluster, even assuming an error on the cluster distance as large as 50 per cent.

#056: A faint 8 arcsec-diameter ring of H_2 emission, possibly associated with Kronberger 2, although the median reddening along this line of sight is $E(B-V) = 3.4$ so that most stars are background to the cluster.

#055: This object appears as a small (7 x 7 arcsec) bipolar in UWISH2 images and is projected within the cluster radius of Kharchenko 2. However it lies close ($\sim$ 2 arcmin) to the western edge of the HII region Sh2-48 and the IR bubble N18 which are associated with ongoing star formation (Ortega et al. 2013; Deharveng et al. 2010). It is coincident with a compact radio source GPSR5 16.600-0.276 (Becker et al. 1994) and was identified as a possible compact HII region by Deharveng et al. (2010). The radio emission is resolved in the 5 GHz CORNISH survey (Purcell et al. 2013) with an integrated flux of 22.2 ± 4.3 mJy, angular scale 4.2 arcsec, and a morphology similar to that seen in H_2 emission. The mid-infrared colours from IRAC photometry (Table 5; Sec. 4) are more typical of PNe than ultra-compact HII regions so we consider this object a likely PN. The extinction map of Rowles & Froebrich (2009) give $E(B-V) = 1.1$ for this object, which is similar to that reported for the cluster. If this is really a PN then this is the most likely candidate for cluster membership in our sample.

Objects projected onto one of the young clusters may be candidate YSO outflows, rather than PNe. Three of the objects are confirmed PNe (T) and two have IRAC colours consistent with PNe (t), so these must be chance alignments. There are a further eight objects; seven candidate PNe (c), and one (#274) which is likely to be associated with the HII region BFS 30.

7 DISCUSSION AND SUMMARY

The 284 PN candidates presented in F15 are supplemented with a further 23 (mostly very faint) H_2 nebulae (Table A2) to give a final list of 307 objects. Cut-out images showing the H_2 emission are given in Appendix B and C and all objects are listed in Table A1 along with their H_2 morphology and dimensions.

Where available we have obtained mid-infrared photometry in the four *Spitzer* IRAC bands to place objects onto diagnostic colour-colour diagrams. This has allowed us to identify 11 objects which are probably not PNe: 5 YSOs, 4 HII regions, 1 symbiotic system and 1 pre-PN (Sec. 4). Adding in 5 objects which have previously been classified as not PNe, there are 16 non-PNe in the sample, leaving a total of 291 PN candidates, 183 of which are new detections. For PN candidates with IRAC colours, we find that they are well-clustered within the regions in the colour-colour planes defined by the 'true' PNe (Fig. 7), showing that our initial selection of objects, based mainly on appearance in H_2 imaging, was largely successful. We have used the classifiers t, l and p, to indicate the likeliness of a PN nature, on the basis of the IRAC colours (Sec. 5 and Table A1).

By searching for H α emission at the location of the UWISH2 sources, in either the SHS or IPHAS surveys, we find that 95 of the 108 previously known PN candidates show H α emission (Figs. B1-B5). This is not surprising given that the main discovery technique for PNe has been by identification in H α surveys. In addition we find 28 objects that appear to be associated with H α emission but which have not been previously noted (Figs. B6-B8). The majority of the new PN candidates identified by their H_2 emission, 155 out of 183, have no detection in H α emission, raising the possibility of a significant population of optically-obscured PNe.

We find in Sec. 3.4 that the spatial distribution of PN candidates with and without detectable H α emission is noticeably different, with there being fewer H α-detected PNe in the inner GP ($l < 20°$) and at lower latitudes ($-1° < b < 1°$). To assess the effects of extinction on the ability to detect PNe at optical wavelengths, we have used the extinction maps of Rowles & Froebrich (2009) to obtain estimates of A_v at the position of each object. We find that, in general, the objects with no detectable H α emission are located in regions with higher extinction than those where H α emission is detected, with median values of $A_v = 5.4$

Downloaded from https://academic.oup.com/mnras/advance-article-abstract/doi/10.1093/mnras/sty1580/5037956
by University of Kent user
on 18 June 2018

Table 5. UWISH2 objects projected onto open clusters showing object number (Table A1) and Galactic coordinates. The cluster id, name, angular radius, estimated distance, colour excess and age (from Kharchenko et al. 2013) are given. Δr_2 is the separation of the PN candidate from the cluster centre in units of r_2. The final column gives the object type, as listed in Table A1. The first 5 objects are projected onto clusters with log (age) > 7.7 Myr.

Object #	l (deg)	b (deg)	MWSC	Cluster	r_2 (deg)	D (pc)	$E(B-V)$	log(t) (Myr)	Δr_2	Type
012	4.76799	-0.85257	2772	Ruprecht 137	0.16	1405	1.124	8.80	0.34	YSO
290	15.46686	1.10391	2858	ASCC 94	0.27	731	0.25	8.84	0.76	c
071	21.74338	-0.67287	2949	NGC 6649	0.18	1564	1.332	8.1	0.82	T
056	16.92321	-0.00616	2898	Kronberger 2	0.14	3197	1.791	8.2	0.77	c
055	16.60078	-0.27565	2900	Kharchenko 2	0.19	3412	1.041	8.43	0.48	t
018	5.90685	-1.37325	2798	NGC 6530	0.2	1365	0.541	6.67	0.89	c
286	6.33697	-0.6148	2781	Bochum 14	0.167	538	1.853	7.1	0.67	c
021	8.33574	-1.10291	2814	ASCC 93	0.165	1830	0.583	6.1	0.38	T
027	10.21147	0.34469	2809	FSR 0039	0.14	2940	0.802	6.0	0.30	T
046	15.13012	-0.44046	2896	NGC 6618	0.29	1308	1.607	6.0	0.88	t
060	18.14941	1.53214	2878	NGC 6604	0.265	1895	0.968	6.89	0.74	T
084	24.89596	0.45853	2957	Dolidze 31	0.115	5163	1.353	6.0	0.77	t
090	26.44767	-0.8084	2977	NGC 6683	0.11	1441	0.333	6.75	0.79	c
117	31.16908	0.81029	2986	Berkeley 79	0.11	2434	1.145	6.8	0.99	c
303	60.02622	-0.28202	3173	Roslund 2	0.18	1668	0.899	6.78	0.77	c
258	75.90338	0.29517	3325	Berkeley 87	0.18	1239	1.353	7.1	0.95	c
274	143.5014	-2.81706	274	Melotte 20	6.1	175	0.09	7.7	0.89	poss HII
278	149.43257	-2.19327	274	Melotte 20	6.1	175	0.09	7.7	0.78	c

and 7.2 mag respectively for the two groups. We also find that objects without detectable H α emission typically have smaller angular extent on the sky than those with detectable H α emission (median surface area of 70 and 160 arcsec^2, respectively), suggesting that the former group are located at greater distance and therefore suffer more extinction. The flux distributions of the two groups are also distinct (Fig. 4), with median fluxes of 9.1 and 3.2×10^{-17} W m^{-2} for objects with and without H α detection. The combined trends of lower flux and smaller angular extent, with greater extinction, suggest that UWISH2 is probing longer sightlines in the GP to detect a population of new and faint objects that are likely to be optically-obscured PN candidates.

We have compared the H α and H_2 surface brightnesses for 23 PNe for which physical radii are available from the $S_{H\alpha}-r$ relationship. Due to the flat trend of S_{H_2} with radius, the H_2 and H α surface brightnesses become comparable for PNe with radii greater than 0.5 pc (Fig. 6). The maximum radius of a visible PN is estimated as 0.9 pc, beyond which it falls below H α detectability at age 21 000±5 000 years (Jacob et al. 2013). It seems likely that older PNe will be more easily detected via their H_2 emission, especially in the GP where extinction at optical wavelengths is high. For PNe which show no detectable H_2 emission then other diagnostics may be useful. The MIPSGAL 24 µm survey is thought to contain many potential PNe (Mizuno et al. 2010) and in some cases the emission is dominated by the [OIV] line at 25.9µm, suggesting that they are high-excitation PNe (Nowak et al., 2014; Flagey et al. 2011).

To assess the PN detection efficiency of UWISH2 we search for known PNe within the area $10^\circ < l < 66^\circ$ and $|b| < 1.5^\circ$ using the HASH database, giving a total of 287 objects. Of these, 85 are detected in UWISH2 (30 per cent). However, if we take only objects with reliable spectroscopic confirmation ('true' PNe) then 61 out of 114 objects (54 per cent) are found in UWISH2 (Sec. 3.3). The probability of detecting H_2 emission from a PN would seem to lie between 30 and 54 per cent. Within the same area we detect 131 PN candidates in UWISH2 which do not appear in H α surveys. Assuming that these objects are all optically-obscured PNe then, with a detection efficiency of 30 or 54 per cent, there would be in total 437 or 243 PNe hidden from H α surveys. Including infrared detections can therefore be expected to significantly increase the number of PN candidates in a given area of sky, especially close to the GP where extinction effects are most severe. In the sample area ($10^\circ < l < 66^\circ$, $|b| < 1.5^\circ$) the number increases from 287 optically-detected PNe to at least 418 (287+131) objects, but up to 724 (287+437). Including near-infrared detections increases PN candidate numbers by a factor between 1.5 and 2.5 within the UWISH2 survey area.

ACKNOWLEDGEMENTS

This paper makes use of data obtained as part of the INT Photometric H α Survey of the Northern GP (IPHAS, www.iphas.org) carried out at the Isaac Newton Telescope (INT). The INT is operated on the island of La Palma by the Isaac Newton Group in the Spanish Observatorio del Roque de los Muchachos of the Instituto de Astrofisica de Canarias. All IPHAS data are processed by the Cambridge Astronomical Survey Unit, at the Institute of Astronomy in Cambridge. This research has made use of: the NASA/IPAC Infrared Science Archive, which is operated by the Jet Propulsion Laboratory, California Institute of Technology, under contract with the National Aeronautics

Downloaded from https://academic.oup.com/mnras/advance-article-abstract/doi/10.1093/mnras/sty1580/5037956
by University of Kent user
on 18 June 2018

and Space Administration; the SIMBAD database, operated at CDS, Stasbourg, France; the HASH PN database at 'hashpn.space'. AMJ acknowledges receipt of a STFC research studentship. We thank the referee for their helpful comments.

REFERENCES

Aleman I., Gruenwald R., 2011, A&A, 528, 74
Barentsen G., et al., 2014, MNRAS, 444, 3230
Becker R.H., White R.L., Helfand D.J., Zoonematkermani S., 1994, ApJS, 91, 347
Beckwith S., Persson S.E., Gatley I., 1978, ApJ, 219, 33
Casali M.M., Eiroa C., 1996, A&A, 306, 427
Choi J., Dotter, A., Conroy C., Cantiello M., Paxton B., Johnson B.D., 2016, ApJ, 823, 102
Cohen M., Parker Q.A., Green A.J., Miszalski B., Frew D., Murphy T., 2011, MNRAS, 413, 514
Cooper H.D.B., et al., 2013, MNRAS, 430, 1125
Davis C.J., Smith M.D., Stern L., Kerr T.H., Chiar J.E., 2003, MNRAS, 344, 262
Deharveng L., et al., 2010, A&A, 523, 6
Drew J.E., et al., 2005, MNRAS, 362, 753
Drew J.E., et al., 2014, MNRAS, 440, 2036
Lucas P.W., et al., 2008, MNRAS, 391, 136
Fang X., Zhang Y., Kwok S., Hsia C-H., Chau W., Ramos-Larios G., Guerrero M., 2018, arXiv:1804.08840
Flagey N., Noriega-Crespo A., Billot N., Carey S.J., 2011, ApJ, 741, 4
Frew D.J., Bojičić I.S., Parker Q.A., Pierce M.J., Gunawardhana M.L.P., Reid W.A., 2014, MNRAS, 440, 1080
Frew D.J., Parker Q.A., 2010, PASA, 27. 129
Frew D.J., Parker Q.A., Bojičić I.S., 2016, MNRAS, 455, 1459
Froebrich D., et al., 2011, MNRAS, 413, 480
Froebrich D., et al., 2015, MNRAS, 454, 2586
Gledhill T.M., Forde K.P., 2015, MNRAS, 447, 1080
Guerrero M.A., Villaver E., Manchado A., Garcia-Lario P., Prada F., 2000, ApJS, 127, 125
Hrivnak B.J., Kwok S., Geballe T.R., 1994, ApJ, 420, 783
Jacob R., Schönberner D., Steffen M., 2013, A&A, 558, 78
Kanarek G., Shara M., Faherty J., Zurek D., Moffat A., 2015, MNRAS, 452, 2858
Kastner J.H., Weintraub D.A., Gatley I., Merrill K.M., Probst R.G., 1996, ApJ, 462, 777
Kharchenko N.V., Piskunov A.E., Schilbach E., Röser S., Scholz R.-D., 2013, A&A, 558, 53
Manchado A., Guerrero M.A., Stanghellini L., Serra-Ricart M., 1996, The IAC Morphological Catalog of Northern Galactic Planetary Nebulae. Instituto de Astrofisica de Canarias (IAC), La Laguna, Spain
Marquez-Lugo R.A., Guerrero M.A., Ramos-Lario G., Miranda L.F.2015, MNRAS, 453, 1888
Megeath S.T., et al., 2012, AJ, 144, 192
Miszalski B., Parker Q.A., Acker A., Birkby J.L., Frew D.J., Kovacevic A., 2008, MNRAS, 384, 525
Mizuno D.R., et al., 2010, AJ, 139, 1542
Nowak M., Flagey N., Noriega-Crespo A., Billot N., Carey S.J., Paladini R., Van Dyk, S.D., 2014, ApJ, 796, 116
Ortega M. E., Paron S., Giacani E., Rubio M., Dubner G., 2013, A&A, 556, 105
Parker Q.A., et al., 2005, MNRAS, 362, 689
Parker Q.A., et al., 2006, MNRAS, 373, 79
Parker Q.A., et al., 2012, MNRAS, 427, 3016
Parker Q.A., Bojičić I.S., Frew D.J., 2016, in Liu X., Stanghellini L., Karakas A., eds, Proc. IAU Symp. 323, Planetary Nebulae:Multi-wavelength Probes of Stellar and Galactic Evolution. Cambridge University Press, p.36
Purcell C.R., et al., 2013, ApJS, 205, 1
Ramos-Larios G., Guerrero M.A., Sabin L., Santamaría E., 2017, MNRAS, 470, 3707
Reipurth B., Aspin C., 1997, AJ, 114, 2700
Rowles J., Froebrich D., 2009, MNRAS, 395, 164
Sabin L., et al., 2014, MNRAS, 443, 3388
Storey J.W.V., 1984, MNRAS, 206, 521
Treffers R.R., Fink U., Larson H.P., Gautier T.N., 1976, ApJ, 209, 793
Urquhart J.S., et al., 2009, A&A, 501, 539
Wang S., Jiang B.W., 2014, ApJ, 788, L12
Zhang Y., Hsia C-H., Kwok S., 2012, ApJ, 745, 59
Zuckerman B., Gatley I., 1988, ApJ, 324, 501

Downloaded from https://academic.oup.com/mnras/advance-article-abstract/doi/10.1093/mnras/sty1580/5037956
by University of Kent user
on 18 June 2018

APPENDIX A: PN CANDIDATE LISTS

Table A1. Morphology, extent and IRAC photometry for UWISH2 PN candidates. Columns are (1) candidate number; (2) UWISH2 ID; (3) morphology and (4) extent of H_2 emission (major x minor axis dimensions in arcsec, or where only one dimension is given it is the major axis); (5) morphology and (6) extent of any H α emission; (7) to (10) IRAC magnitudes and errors; (11) object type: where an existing classification (TLP) exists then this is preserved. For new objects: t, l, p, c indicates "true", "likely", "possible" or "candidate" PN status based on the IRAC colours where photometry in 4, 3, 2 or $\leqslant 1$ bands is available, respectively.

No.	UWISH2 ID	H_2		H α		IRAC mag.				Type
		Morph.	Size	Morph.	Size	[3.6]	[4.5]	[5.8]	[8.0]	
001	000.81878-0.04944	Ear	5x4			12.42 ± 0.10	11.34 ± 0.07	9.80 ± 0.06	8.08 ± 0.04	t
002	001.22588+0.56414	Ear	3.0x2.6							c
003	001.42213-0.61357	Bamr	22x12							c
004	001.65056+0.18803	Barm	26x13	E	12x6	12.34 ± 0.10	11.83 ± 0.09	10.82±0.11	9.59±0.11	T
005	001.72196-0.82262	Eamr	20x12							c
006	001.73118+0.44232	Brs	8x5							c
007	002.03824-0.34363	Ear	34x18							c
008	002.25319+0.55724	Ears	30x20	Eprs	38x12					T
009	003.65197-0.25068	Ear	7x5							c
010	003.79367-0.81428	Ear	4x3							c
011	004.44847-0.21905	Ims	120x90							c
012	004.76799-0.85257	Bams	25x12			12.71 ± 0.11	12.27 ± 0.11	12.13 ± 0.22	11.45 ± 0.44	YSO
013	004.88887-0.58981	Is/B	34x12	Ias/B	88x62					T
014	004.99841-0.72107	A	9x4			9.88 ± 0.02	9.71 ± 0.03	9.53 ± 0.05	9.56 ± 0.15	YSO?
015	005.14078+0.58616	Rar	7							c
016	005.42811-0.16852	Bms	40x9	B	10x3				8.03 ± 0.04	c
017	005.56222-0.15023	Rar	7							c
018	005.90685-1.37325	Ear	8x5							c
019	006.51856-0.69279	Ear	10x6							c
020	006.73073-1.19177	Bas	9x6			12.66 ± 0.15	12.03 ± 0.12	12.05 ± 0.35	10.01 ± 0.17	t
021	008.33574-1.10291	Is	35	Emps	30x20					T
022	008.36142-0.62384	Bmps	8x6							c
023	008.94169+0.25318	Ears	20x10	Er	27x11				11.94 ± 1.50	L
024	009.76150-0.95756	Bs	18x6			11.97 ± 0.07	9.98 ± 0.03	9.11 ± 0.03	7.29 ± 0.02	t
025	009.80708-1.14613	Bmps	36x14	Bms	32x12	11.82 ± 0.08	10.32 ± 0.04	9.27 ± 0.05	7.51 ± 0.03	T
026	010.10373+0.73752	Bmps	140x36	Bmps	11x10	7.66 ± 0.01	5.99 ± 0.00	4.80 ± 0.00	2.80 ± 0.00	T
027	010.21147+0.34469	Brs	56x20	Bams	61					T
028	010.26120-0.79452	Bmr	12x7			2.02 ± 0.06	11.77 ± 0.10	10.33 ± 0.15	8.91 ± 0.11	t
029	010.39239+0.53966	Emr	24x13			8.08 ± 0.01	7.49 ± 0.01	5.19 ± 0.00	3.54 ± 0.00	HII
030	010.94194-0.40277	Bas	15x13			12.09 ± 0.12	10.99 ± 0.07	10.91 ± 0.22	8.69 ± 0.10	t
031	011.00185+1.44395	Bas	26x16	E	19x17	10.74 ± 0.05	9.92 ± 0.03	8.79 ± 0.03	6.88 ± 0.02	T
032	011.32982+0.54981	B	11x5			9.66 ± 0.03	9.34 ± 0.03	9.30 ± 0.06	8.44 ± 0.08	YSO?
033	011.45829+1.07349	Ar	6x3.5							P
034	011.52915+1.00385	R	9	E	6.5x6.0					P
035	011.86338+0.30190	E	10x8							c
036	012.11515+0.07516	Bbs	22x10			10.11 ± 0.02	9.07 ± 0.02	8.79 ± 0.03	6.93 ± 0.02	L
037	012.20907+0.43081	I	11x5							c
038	012.21971-0.33477	Bp	16x5	A	20x10	13.89 ± 0.27	13.67 ± 0.31	11.25 ± 0.13	9.12 ± 0.12	HII
039	012.71728+0.37202	Bp	14x10			12.59 ± 0.21	11.19 ± 0.11	10.82 ± 0.22	9.01 ± 0.11	t
040	012.80348+0.00510	Er	16x14							c
041	013.61090+1.01274	Ear/Be	13x8	R	13x13		11.69 ± 0.08		10.08 ± 0.19	p
042	014.58523+0.46161	B	9x4	Ea	6x5	9.76 ± 0.02	8.65 ± 0.01	8.53 ± 0.02	6.36 ± 0.01	L
043	014.64501+0.08920	Ba	14x8	E	20x10	10.97 ± 0.05	10.59 ± 0.06	8.81 ± 0.04	6.91 ± 0.02	t
044	014.65833+1.01220	Ears	22x20	Eas	30x22					T
045	014.92112+0.06989	Ers	30x16	R	8	7.06 ± 0.01	6.71 ± 0.01	4.07 ± 0.00	2.51 ± 0.00	HII
046	015.13012-0.44046	Bas	40x20			11.19 ± 0.07	10.02 ± 0.05	9.33 ± 0.07	7.66 ± 0.05	t
047	015.53753-0.01923	Er	35x7	Emr	55x11					L
048	015.54859-1.00657	Bps	12x3			8.89 ± 0.01	8.13 ± 0.01	5.92 ± 0.01	4.25 ± 0.00	HII
049	015.67993-1.36320	Ear	12x10							c
050	016.02790-1.00525	Rar	7							c
051	016.11984-0.98789	B	30x15							c
052	016.17480+1.37914	Bp	24x10							c
053	016.41571-0.93047	Bpr	54x32	Bps	30x18					T
054	016.48834-1.36082	Is	45x40							c
055	016.60078-0.27565	Bs	7x7			12.11 ± 0.12	10.91 ± 0.06	11.00 ± 0.18	8.70 ± 0.08	t
056	016.92321-0.00616	Rar	8							c
057	017.22288+0.12645	Bs	36	B	20x6					L
058	017.58861+1.09048	Bas	9x4	S		13.23 ± 0.17	12.08 ± 0.09	12.29 ± 0.26	9.97 ± 0.15	t
059	017.61528-1.17013	As/Bas?	240	E/B		7.23 ± 0.01	6.58 ± 0.01	5.52 ± 0.01	4.12 ± 0.01	T

Downloaded from https://academic.oup.com/mnras/advance-article-abstract/doi/10.1093/mnras/sty1580/5037956
by University of Kent user
on 18 June 2018

Table A1. continued.

No.	UWISH2 ID	H_2		H α		IRAC mag.				Type
		Morph.	Size	Morph.	Size	[3.6]	[4.5]	[5.8]	[8.0]	
060	018.14941+1.53214	Bps	16x10	Bams	16x11					T
061	018.41760-0.10793	B	16x12							c
062	018.83207+0.48278	R	3.5			14.50 ± 0.32	13.44 ± 0.22	12.51 ± 0.32	11.64 ± 0.44	t
063	020.46958+0.67836	Rar	40	B/R	8x7	10.22 ± 0.02	9.15 ± 0.02	8.55 ± 0.02	6.28 ± 0.01	T
064	020.70907-0.17267	Bs	14x9	A	15x9	12.28 ± 0.12	11.80 ± 0.14			p
065	020.80590-0.57267	Bprs	36x16							c
066	020.85450+0.48588	B	2.8x1.2			10.08 ± 0.02	7.49 ± 0.01	5.54 ± 0.00	4.12 ± 0.00	pre-PN
067	020.97795+0.92363	Bms	35x5	E	10x8	11.47 ± 0.04	10.36 ± 0.03	9.76 ± 0.04	7.82 ± 0.02	L
068	020.98141+0.85244	Is	35x16	Aa	47x11				8.95 ± 0.14	L
069	021.29383+0.98091	Is/Bs	>60	Bs	54x42					T
070	021.30767-0.25089	Is	25x25							c
071	021.74338-0.67287	Brs	22x7	B	12x9	12.17 ± 0.11	11.23 ± 0.09	10.44 ± 0.15	9.22 ± 0.15	T
072	021.81951-0.47837	Bprs	52x12	Bp	24x12	10.61 ± 0.04	9.85 ± 0.04	8.73 ± 0.06	6.44 ± 0.03	T
073	022.44734-0.44228	Ears	32x26							c
074	022.57000+1.05505	Brs	22x15	Bs	23x17	10.55 ± 0.03	9.79 ± 0.03	9.20 ± 0.04	7.24 ± 0.02	T
075	022.99501-0.56968	I	10x6							c
076	022.99982+0.10714	Bps	40x22							c
077	023.44011+0.74528	Bs	10x5	Eas	13x9	11.99 ± 0.09	10.91 ± 0.06	10.69 ± 0.13	8.68 ± 0.08	T
078	023.78286+0.50238	Bp	6x3						7.10 ± 0.05	c
079	023.89021-0.73778	Bs	25x14			9.90 ± 0.02	8.32 ± 0.01	7.42 ± 0.01	5.56 ± 0.01	P
080	023.90016-1.28024	Brs/Ers	18x10	Ers	12x9					T
081	024.58540+0.11989	Bs	10x3	S		15.20 ± 0.82	14.10 ± 0.54			p
082	024.76272-0.91396	Bs	3.4x2.2			14.22 ± 0.24	13.51 ± 0.20	12.89 ± 0.46	11.10 ± 0.29	t
083	024.77483-1.31616	Ars	10							c
084	024.89596+0.45853	Bs	14x6			10.69 ± 0.04	9.32 ± 0.02	8.31 ± 0.02	7.06 ± 0.02	t
085	025.66408+1.15020	As	46	As	41x22				8.25 ± 0.08	P
086	025.77993-0.44005	Rrs	4.5x3.5			14.00 ± 0.22	12.79 ± 0.13	12.53 ± 0.40	10.37 ± 0.18	p
087	025.92671-0.98449	Bps	13x5	B	4.6	12.07 ± 0.07	11.23 ± 0.05	10.51 ± 0.08	8.65 ± 0.05	T
088	025.99096-0.59183	Ers	8x5						11.27 ± 0.39	c
089	026.42837+1.03759	Bps	7x6			13.63 ± 0.21	12.19 ± 0.09	12.05 ± 0.21	10.30 ± 0.18	t
090	026.44767-0.80840	Bps	10x5							c
091	026.74999-1.21865	Ers	18x12	Ear	15x13					T
092	026.79572-1.05024	Bs	4x3	E	13x10	13.42 ± 0.16	11.78 ± 0.07	11.16 ± 0.10	9.28 ± 0.06	T
093	026.83269-0.15180	Bs	9x3	E	7x5	11.55 ± 0.06	10.87 ± 0.06	10.36 ± 0.12	8.78 ± 0.09	T
094	026.83640+0.28828	Ers	6x4							c
095	027.09954+0.94886	Es	12x9							c
096	027.37280+1.39262	Ear	7.5x6.0	R	7					c
097	027.66357-0.82670	Bps	14x5.2	Bmp	35x12	12.37 ± 0.08	10.91 ± 0.04	9.68 ± 0.04	7.65 ± 0.02	T
098	027.70327+0.70354	Rars	52x40	Es	15x12	9.76 ± 0.02	8.65 ± 0.01	8.53 ± 0.02	6.36 ± 0.01	T
099	027.81843-0.76628	Bs	8x4	S		12.66 ± 0.11	11.97 ± 0.09	11.74 ± 0.17	9.80 ± 0.13	T
100	028.06295-0.61048	Rr	6							c
101	028.19767-0.89109	B	14x8							c
102	028.52225-1.48422	Rars	30x30	Bam	44x42					T
103	028.62122-0.86537	Rr	10							c
104	028.89451-0.29151	Bs	50x7	As	51x30					T
105	029.21554+0.02262	B	30x12							c
106	029.50204+0.62395	B	25x12	Bm	24x13					T
107	029.57883-0.26901	Bs	6x3	Sm	4	9.36 ± 0.02	8.43 ± 0.01	7.51 ± 0.02	5.82 ± 0.01	L
108	029.99765+0.65621	B	110x40							c
109	030.04497+0.03465	Ers	36x24	Rar	36					T
110	030.17049+0.68782	Ers	5.4x3.2							c
111	030.22594+0.54285	As	15x15			9.21 ± 0.02	8.96 ± 0.02	9.07 ± 0.06	8.12 ± 0.07	YSO?
112	030.30097-1.22812	Bs	9x5							c
113	030.50743-0.21913	Bs	29x18	Bs	35x33					T
114	030.66759-0.33136	Bs	15x10			9.46 ± 0.02	7.29 ± 0.01	5.97 ± 0.01	3.78 ± 0.00	c
115	030.72160+0.14788	Bs	18x17							c
116	030.76828+1.40983	B	4x2.5							c
117	031.16908+0.81029	R	3.5							c
118	031.32618-0.53286	Brs	22x11	Baprs	34x28	13.07 ± 0.39	11.64 ± 0.20	10.73 ± 0.28	8.71 ± 0.15	T
119	031.63781+0.99595	Rr	6							c
120	031.90685-0.30936	Bs	40x25	Bmps	69x42					T
121	032.14993+0.64445	Bs	9x5							c
122	032.22860-1.44045	Es	26x26	Bmps	47x45					T

Downloaded from https://academic.oup.com/mnras/advance-article-abstract/doi/10.1093/mnras/sty1580/5037956
by University of Kent user
on 18 June 2018

Table A1. continued.

No.	UWISH2 ID	H_2		H α		IRAC mag.				Type
		Morph.	Size	Morph.	Size	[3.6]	[4.5]	[5.8]	[8.0]	
123	032.28479-0.27816	Bs	12x8			12.73 ± 0.22	12.24 ± 0.20	11.75 ± 0.46	9.87 ± 0.28	t
124	032.29224-0.74568	As	5.4x2.6			12.68 ± 0.10	12.25 ± 0.11	11.69 ± 0.20	12.08 ± 0.94	YSO?
125	032.37721-0.55490	Bps	14x7	R	5	13.45 ± 0.23	12.53 ± 0.14	11.43 ± 0.19	9.48 ± 0.12	T
126	032.46866+0.28147	Bs	4x2			13.38 ± 0.18	12.46 ± 0.14	12.25 ± 0.36	10.88 ± 0.34	t
127	032.54650-0.03210	Bps	28x14	B	15x11					T
128	032.54998-0.29529	Bps	16x12	E	15x12	12.00 ± 0.11	11.75 ± 0.13	10.80 ± 0.19	8.93 ± 0.11	T
129	032.61348+0.79678	B	5.6x4.0	S		13.38 ± 0.18	12.46 ± 0.14	12.25 ± 0.36	10.88 ± 0.34	P
130	032.66916-1.25559	Bps	12x5	E	10x5					T
131	032.94004-0.74662	Bs	6x4	E	7x5	12.12 ± 0.07	11.67 ± 0.07	11.21 ± 0.13	9.03 ± 0.06	T
132	033.16509+0.49150	Bs	6x3			13.45 ± 0.16	12.92 ± 0.14	11.40 ± 0.14	10.05 ± 0.16	t
133	033.45470-0.61500	As	5x2.5	S	3.5	-				T
134	033.88796+1.52134	Bm	38x20	Bas	51x37					T
135	033.97946-0.98557	Er	10x8	Ers	8x7					T
136	034.10462-1.64333	Es	10x7	Es	10x8					T
137	034.41021+0.81477	Es	5x2			14.35 ± 0.30	13.27 ± 0.22	12.91 ± 0.50	11.18 ± 0.36	t
138	034.84509+1.31721	Bs	14x7			13.60 ± 0.16	12.39 ± 0.10			L
139	035.18522+1.12134	Ems	12x9			13.18 ± 0.18	12.12 ± 0.11			p
140	035.23366-1.13623	Ers	60x50							c
141	035.38919-1.17506	Bs	7.5x6							c
142	035.47394-0.43716	Bs	25x15	B	16x10	8.48 ± 0.01	7.29 ± 0.01	5.71 ± 0.00	4.08 ± 0.00	t
143	035.76967-1.24531	Bs	26x12							L
144	035.81426+1.48019	As	9x7							c
145	035.81489-0.25181	Bs	25x20							P
146	035.89918-1.14425	Ers	7x6							c
147	036.05309-1.36593	Bms	300x90	Bmps	270x120					T
148	036.43225-1.91396	Bps	14	Bmp	21					Sym?
149	036.46081+0.80581	Er	14x9							c
150	036.48189+0.15610	Bps	12x5			12.91 ± 0.14	11.96 ± 0.10	10.93 ± 0.12	9.52 ± 0.13	t
151	036.98479-0.20330	Rrs	12			13.40 ± 0.21	12.07 ± 0.12	11.16 ± 0.17	9.73 ± 0.15	t
152	037.14125+0.30341	E	10x7							c
153	037.41544-0.19254	Er	6x5			13.03 ± 0.13	11.87 ± 0.09	10.99 ± 0.15	9.51 ± 0.11	t
154	037.96134+0.45337	Bp	11x3.5			11.30 ± 0.04	9.79 ± 0.03	8.17 ± 0.02	6.21 ± 0.01	L
155	038.14463-0.57489	A	10x8							c
156	038.83959+0.87057	E	8x6							c
157	039.16222+0.78375	B	12x6			11.29 ± 0.04	10.35 ± 0.03	8.99 ± 0.03	7.14 ± 0.02	t
158	039.26101-0.55123	Bs	30x20							c
159	039.64158-0.36822	Bs	5x2.5			11.28 ± 0.04	10.30 ± 0.03	10.09 ± 0.07	8.99 ± 0.06	t
160	040.03148-1.30313	Ear	30x20	R?	2.5					c
161	040.36950-0.47517	Rrs	35x32	Rrs	31	9.76 ± 0.02	8.65 ± 0.01	8.53 ± 0.02	6.36 ± 0.01	T
162	040.47073+1.10067	Bs	12x4			12.15 ± 0.07	10.92 ± 0.05		7.54 ± 0.02	l
163	040.53948-0.76310	Bs	12x7			13.54 ± 0.21	11.94 ± 0.09	10.82 ± 0.12	9.93 ± 0.18	t
164	040.96700-1.22601	Ears	80x50							c
165	041.27043-0.69797	Bas	30x15	Bs	18	12.12 ± 0.07	11.67 ± 0.07	11.21 ± 0.13	9.03 ± 0.06	T
166	041.99634+0.10743	B	35x25						8.45 ± 0.14	c
167	042.12631+0.45706	Bs	9x9			13.24 ± 0.18	12.21 ± 0.12	11.54 ± 0.23	9.84 ± 0.14	t
168	042.97101-1.07103	As	7x5							c
169	043.10420-1.70207	Bs	12x8							c
170	043.25830+1.50423	Es	3.5x2.5	As	5x2	15.23 ± 0.33	14.31 ± 0.24			p
171	043.65562-0.82777	Rs	5	S		10.65 ± 0.03	10.18 ± 0.03	7.99 ± 0.01	6.31 ± 0.01	HII
172	044.18877+1.56732	Is	140x120	R	3					T
173	044.34714+0.08637	Ear	9x8			13.21 ± 0.15	12.59 ± 0.13	12.14 ± 0.36	10.06 ± 0.19	t
174	044.73433+0.26046	Bps	25x12	B	15x9	11.09 ± 0.04	10.41 ± 0.04	9.77 ± 0.05	8.11 ± 0.05	T
175	044.93245-0.01060	Bms	40x25	Bamp	35x20					T
176	045.44425-1.57085	Rr	14							c
177	045.45878-0.49801	Bas	25x13							c
178	045.95707+0.69049	Is	26x17							c
179	046.09523+1.36603	Ers	9x5	B	9x7					c
180	046.63335+1.31220	As	16x10	B?	7	11.63 ± 0.04	11.35 ± 0.05			p
181	046.93735-0.54973	Br	8x5			14.04 ± 0.23	13.35 ± 0.19	12.13 ± 0.25	11.04 ± 0.30	t
182	047.18522+0.44999	Brs	25x14	S?				11.18 ± 0.08	9.16 ± 0.08	p
183	047.44521+0.61199	Es	11x8							c
184	047.50612-0.36750	Es	12x8			13.99 ± 0.27	12.70 ± 0.15	11.34 ± 0.16	10.47 ± 0.22	t

Downloaded from https://academic.oup.com/mnras/advance-article-abstract/doi/10.1093/mnras/sty1580/5037956
by University of Kent user
on 18 June 2018

Table A1. continued.

No.	UWISH2 ID	H_2		H α		IRAC mag.				Type
		Morph.	Size	Morph.	Size	[3.6]	[4.5]	[5.8]	[8.0]	
185	047.52536+0.32144	Ears	7x5							c
186	047.61228+1.08168	Ers	13x11	Ears	16x12					T
187	048.03497+0.12296	Bas	7x6							c
188	048.24968-0.46947	Bs	10x8				13.04 ± 0.22		11.26 ± 0.53	p
189	048.71570-0.28960	Bs	44x24	B	13x7					T
190	048.99884+0.77703	Rrs	8x8			13.29 ± 0.13	12.24 ± 0.09	11.69 ± 0.14	9.93 ± 0.15	t
191	049.28561+0.00740	Brs	24x16	Ear	18x13					T
192	049.86763+1.06075	As	30x20	A?	25x17					c
193	049.91632-1.08675	Es	11x8							c
194	050.04556-0.79804	Bs	12x12				12.31 ± 0.10	11.69 ± 0.21	10.42 ± 0.20	l
195	050.48027+0.70434	Bs	16x8	B	14x6	7.02 ± 0.00	6.03 ± 0.00	5.17 ± 0.00	4.56 ± 0.00	Sym?
196	050.55559+0.04506	Bs	16x5	S		9.73 ± 0.02	8.84 ± 0.02	7.61 ± 0.01	5.78 ± 0.01	L
197	050.66579+1.33631	B	6x3.5	E	6x5					T
198	050.66912+0.00673	A	22x26	Ea	23					T
199	050.71285-0.17840	B	6x3			11.52 ± 0.04	10.58 ± 0.03	10.89 ± 0.10	8.86 ± 0.05	t
200	050.78036+1.18512	Ra	50x20	R?	2.5					c
201	050.90936+1.05076	As	5			8.21 ± 0.01	7.98 ± 0.01		4.91 ± 0.01	l
202	050.92866+0.43874	Eas	11x7							c
203	051.36290+0.87878	Rars	6			13.64 ± 0.15	12.59 ± 0.11	11.99 ± 0.16	10.52 ± 0.14	t
204	051.50791+0.17037	Er	12x10	Emrs	13x9	9.57 ± 0.02	8.66 ± 0.01	7.63 ± 0.01	5.61 ± 0.01	T
205	051.76939+1.36491	Ears	26	Ears	30x20					T
206	051.83306+0.28374	E	54x30	E	20x16	10.58 ± 0.03	9.46 ± 0.02	9.02 ± 0.03	7.03 ± 0.02	T
207	052.32654-0.13737	Eas	8x6							c
208	052.46943-0.90047	Bs	9x5			13.96 ± 0.20	12.79 ± 0.11	11.89 ± 0.17	9.98 ± 0.13	t
209	052.70187-1.04355	A	25x12							c
210	053.04316-0.06957	Bas	4x3			13.38 ± 0.20	13.27 ± 0.24	12.35 ± 0.38	11.13 ± 0.40	t
211	053.36023-0.54988	Ear	12x6							c
212	054.29190-0.23778	Brs	30x10							c
213	054.71154+0.41990	Bs	20x14	Ba	19x12					T
214	055.50747-0.55729	E	20x14	E	17x13	8.95 ± 0.01	7.94 ± 0.01	6.83 ± 0.01	4.68 ± 0.00	T
215	055.85017+1.44210	I	10x8			10.02 ± 0.02	9.53 ± 0.02			p
216	056.16673-0.41918	Bas	36x22	Bas	40x30?					T
217	056.34479-1.53764	Bas	25x16	B?	28x16					c
218	056.42331-0.37341	Bas	18x12	Ias	31	12.79 ± 0.17	11.38 ± 0.07	11.49 ± 0.26	9.29 ± 0.14	L
219	056.48535-0.09364	Ear	5x2.5							c
220	056.52321+0.30702	Rr	9							c
221	056.61303-0.04761	E	20x13							c
222	057.32913+0.61698	Ear	9x8							c
223	057.59474+0.50715	Is	70x40							c
224	057.64365+0.47814	B	8x4							c
225	057.72078+0.12541	Ear	17x13							c
226	057.81415+0.78641	Bs	16x6							c
227	057.83552+1.04920	Ears	22x15	R	21				10.30 ± 0.31	P
228	057.98004-0.76740	Brs	26x20	B	27x30	12.12 ± 0.11	10.98 ± 0.06	10.02 ± 0.07	8.73 ± 0.08	T
229	058.03770-0.04866	Ir	16x7							c
230	058.17873-0.81177	Bs	20x12	B	15x12	13.01 ± 0.18	12.19 ± 0.10	11.85 ± 0.29	10.38 ± 0.24	L
231	058.80916+0.38692	Bs	20x20							c
232	059.18828-1.42144	A	20	Ras	27					L
233	059.36328+1.00137	Er	25x20	R?	25					c
234	059.77812-0.82788	Bs	12x9	Ea	13x9	9.41 ± 0.02	9.30 ± 0.02	9.08 ± 0.03	8.55 ± 0.04	L
235	059.87554-0.60874	Bas	34x20	Bas	54x30					T
236	060.24810+0.82261	Bps	35x14	B	7x6	12.64 ± 0.09	11.34 ± 0.05	10.72 ± 0.07	8.96 ± 0.05	T
237	060.31487+0.79769	Bs	5x2.5	S?		14.15 ± 0.16	13.51 ± 0.14	11.59 ± 0.11	9.82 ± 0.07	t
238	060.40130+0.97372	A	16x8							c
239	060.52372-0.31828	Bps	11x6	Bs	11x6	12.62 ± 0.09	11.98 ± 0.08	10.97 ± 0.10	9.47 ± 0.07	T
240	060.79926+1.17327	R	8	R?	5.5		14.79 ± 0.54			c
241	061.84215+0.88506	Bs	12x13	B?	12x12	12.92 ± 0.09	12.60 ± 0.11	12.26 ± 0.19	10.52 ± 0.19	t
242	061.91270+0.20109	Ear	11x10							c
243	062.07780-0.43633	Ear	24x12							c
244	062.13719+0.14857	Ear	12x10	E?	10x8	12.96 ± 0.10	12.25 ± 0.10	11.49 ± 0.14	10.37 ± 0.15	t
245	062.15368+1.15140	E	14x11							c
246	062.29042+1.13629	Bs	16x10	E?	11	12.83 ± 0.11	11.92 ± 0.07		9.80 ± 0.10	l
247	062.45283-0.01779	Bs	14x18							c

Downloaded from https://academic.oup.com/mnras/advance-article-abstract/doi/10.1093/mnras/sty1580/5037956
by University of Kent user
on 18 June 2018

Table A1. continued.

No.	UWISH2 ID	H_2		H α		IRAC mag.				Type
		Morph.	Size	Morph.	Size	[3.6]	[4.5]	[5.8]	[8.0]	
248	062.49346-0.27008	Bms	70x18	Bms	90x25	11.87 ± 0.06	10.75 ± 0.04	10.15 ± 0.05	8.20 ± 0.04	T
249	062.70165+0.06019	Bs	17x8	Bps	13x7	11.19 ± 0.04	10.68 ± 0.04	10.25 ± 0.06	8.82 ± 0.07	T
250	062.75413-0.72565	Bs	80x10	B	30x10	12.06 ± 0.05	10.56 ± 0.03	9.60 ± 0.04	7.95 ± 0.03	L
251	062.97476+1.38380	Br	15x9	B	14x8					T
252	063.92454-1.21740	Bs	26x16	Bamps	100x80					T
253	064.13697-0.97667	Bprs	20x20	Bars	33x17					T
254	064.18792+0.77438	Bs	11x4.5	E?	2.3x4	13.28 ± 0.13	12.58 ± 0.11	11.32 ± 0.11	10.46 ± 0.15	t
255	064.29941-0.14559	Bas	40x24	Ears?	23x20					c
256	064.94759+0.76048	Brs	10x8	B?	10x8.5				12.20 ± 0.39	c
257	065.54459+0.81855	Br	24x7							c
258	075.90338+0.29517	Rr	2.8							c
259	076.37264+1.17216	Bprs	44x30	Bprs	42x2					T
260	076.88532+2.22199	Bps	7x4			14.50 ± 0.38	13.74 ± 0.30			p
261	077.65952-0.98321	E	20x17							c
262	077.68068+3.12797	Bps	40x6	Bs	22x5	11.52 ± 0.05				L
263	077.77375+1.55436	R	5							c
264	077.84010+0.86042	Bs/Is	20x15							c
265	078.92993+0.76378	Ras	11x10	Ras	12x11					T
266	079.33319+2.14863	E	8x5							c
267	079.62439+0.40225	Bp	26x12							c
268	079.77014+1.89347	R	8							c
269	080.26214+0.24219	Bs	6x4	E?	7x6					c
270	081.70275+2.15524	Ear	12x5							c
271	082.02890-0.30589	A	15x10							c
272	084.20031+1.09069	Brs	70x45	Bmrs	90x43					T
273	084.68426-0.72166	Rr	9							c
274	143.50140-2.81706	Brs	90x40	Brs	170x90					HII
275	144.15931-0.50100	Ears	24x20	Rar	21x25					T
276	146.29327+0.54871	R	6			10.31 ± 0.02	9.92 ± 0.02			HII?
277	149.16730-0.22038	R	12							c
278	149.43257-2.19327	Ers	15x13	E?	17x13					c
279	151.30910-0.74888	S	3			11.63 ± 0.04	10.48 ± 0.03			p
280	153.77044-1.40652	Bps	7x5	Es	6.7x6.0					T
281	357.65660+0.26265	Ear	6x5							c
282	358.23394-1.18468	Bms	30x17	B	27x20	11.23 ± 0.07	10.16 ± 0.05	9.16 ± 0.06	7.82 ± 0.06	T
283	358.25962-1.91267	I	6x5	S?		8.24 ± 0.01	7.49 ± 0.01	7.02 ± 0.01	6.39 ± 0.01	Sym?
284	359.35683-0.98000	Bps	50x14	Bmps	60x25	7.23 ± 0.01	6.15 ± 0.00	4.58 ± 0.00	2.51 ± 0.00	T
285	000.26373-0.19745	Eas	20x14							c
286	006.33697-0.61480	Ea	7x5							c
287	009.20083-1.37007	Bas	50x20							c
288	010.03253+0.91443	Ba	8x5							c
289	011.32349-1.66821	Ra	26							c
290	015.46686+1.10391	B	5x3							c
291	018.86276+0.65375	B	9x4							c
292	019.77912-0.85302	E	8x4							c
293	022.28851-0.06156	B	7x5							c
294	027.85065-0.64690	E	12x8							c
295	030.25432+1.53745	B	5x3	Ers	7x5	13.22 ± 0.13	11.73 ± 0.06	11.42 ± 0.09	10.12 ± 0.11	L
296	030.84096+0.07624	Es	25x20							c
297	032.37928-0.51843	Ba	8x3							c
298	033.60731+0.94113	Bas	17x12			12.90 ± 0.14	12.10 ± 0.10	11.29 ± 0.14	10.01 ± 0.17	t
299	035.08538-0.53884	Es	4.5x3							c
300	044.60870-0.36523	B	4.5x3							c
301	044.67282-0.98346	Bp	17x6							c
302	051.75061+0.05155	B	16x6							c
303	060.02622-0.28202	Bps	7x3.5							c
304	063.19875+1.14092	Bs	18x8							c
305	064.12864+0.14814	Bs	15x6							c
306	078.65278+3.53770	E	26x15							c
307	081.12354+1.23547	Bas	19x11							c

Downloaded from https://academic.oup.com/mnras/advance-article-abstract/doi/10.1093/mnras/sty1580/5037956
by University of Kent user
on 18 June 2018

Table A2. H_2 features conisdered possible PNe and which are additional to those in Table B1 of F15. Columns are (1) the UWISH2 source ID with the Galactic coordinates, (2) decimal RA and (3) decimal Dec of the geometric centre of the H_2 feature, (4) radius enclosing the H_2 emission, (5) area covered by H_2 emission, (6) total and (7) median H_2 flux, (8) other identifier or comment.

UWISH2 ID	RA [deg]	DEC [deg]	Radius [arcsec]	Area [arcsec^2]	$F_{\rm tot}$ [10^{-19} W m^{-2}]	$F_{\rm med}$	Other ID
000.26373-0.19745	266.75411	-28.81354	14.8	253.29	2781.84	1441.22	
006.33697-0.61480	270.58274	-23.78468	6.4	38.86	171.51	167.487	
009.21329-1.36581	272.81301	-21.63926	49.5	330.06	1236.46	1218.34	
010.03253+0.91443	271.10781	-19.81514	9.1	72.41	270.59	255.61	
011.32349-1.66821	274.17547	-19.93079	10.1	71.48	238.36	217.38	
015.46686+1.10391	273.68854	-14.96764	3.7	26.00	119.46	125.58	
018.86358+0.65383	275.74921	-12.18806	6.9	20.90	61.61	64.28	
019.77912-0.85302	277.54931	-12.08032	5.5	16.31	21.71	3.54	
022.28851-0.06156	278.01694	-9.48958	5.1	31.28	109.98	108.23	
027.85065-0.64690	281.11497	-4.81676	8.7	72.76	292.47	264.85	
030.25432+1.53745	280.26926	-1.68065	3.2	15.43	57.72	52.31	PN G030.2+01.5
030.84096+0.07624	281.83781	-1.82613	10.8	76.02	372.25	207.535	
032.37928-0.51843	283.06890	-0.72829	5.7	53.88	274.83	7252.70	
033.60731+0.94113	282.32974	+1.03010	12.0	201.31	1293.18	841.476	
035.08538-0.53884	284.32148	+1.67049	2.7	13.71	56.61	56.3481	
044.60870-0.36523	288.57179	+10.20750	3.5	16.01	44.58	40.67	
044.67282-0.98346	289.15792	+9.97660	4.9	26.42	68.82	63.67	
051.75061+0.05155	291.64503	+16.70811	6.0	34.56	136.74	126.14	
060.02622-0.28202	296.25780	+23.77211	8.0	58.69	183.26	168.44	
063.19875+1.14092	296.65712	+27.23026	3.9	20.48	48.24	44.65	
064.12864+0.14814	298.15198	+27.52725	7.0	51.06	126.79	111.82	
078.65278+3.53770	304.10530	+41.61373	12.9	122.8	343.84	369.86	
081.12354+1.23547	308.54931	+42.30322	11.2	161.89	451.45	422.53	

Downloaded from https://academic.oup.com/mnras/advance-article-abstract/doi/10.1093/mnras/sty1580/5037956
by University of Kent user
on 18 June 2018